

# Scenario and Model Dependence of Strategic Solar Climate Intervention in CESM

John T. Fasullo<sup>1,1</sup> and Jadwiga H. Richter<sup>1,1</sup>

<sup>1</sup>National Center for Atmospheric Research (UCAR)

January 20, 2023

## Abstract

Model dependence in simulated responses to stratospheric aerosol injection (SAI) is a major uncertainty surrounding the potential implementation of this solar climate intervention strategy. We identify large differences in the aerosol mass latitudinal distributions between two recently produced climate model SAI large ensembles, despite using similar climate targets and controller algorithms, with the goal of understanding the drivers of such differences. Using a hierarchy of recently produced simulations, we identify three main contributors including: 1) the rapid adjustment of clouds and rainfall to elevated levels of carbon dioxide, 2) the associated low-frequency dynamical responses in the Atlantic Meridional Overturning Circulation, and 3) the contrasts in future climate forcing scenarios. Each uncertainty is unlikely to be significantly narrowed over the likely timeframe of a potential SAI deployment if a 1.5C target is to be met. The results thus suggest the need for significant flexibility in climate intervention deployment in order to account for these large uncertainties in the climate system response.

## Scenario and Model Dependence of Strategic Solar Climate Intervention in CESM

J. T. Fasullo<sup>1</sup> and J. H. Richter<sup>1</sup>

<sup>1</sup>National Center for Atmospheric Research, Boulder, CO, 80301.

Corresponding author: Dr. John Fasullo ([fasullo@ucar.edu](mailto:fasullo@ucar.edu))

Key Points:

- A substantial contrast in the meridional structure of stratospheric aerosols exists in two recent climate intervention experiments.
- Differences in the representations of clouds and the Atlantic Meridional Overturning Circulation are identified as key drivers of the contrast.
- The results portend significant uncertainty in the distribution of sulfate gas injections associated with strategic climate intervention.

Abstract

Model dependence in simulated responses to stratospheric aerosol injection (SAI) is a major uncertainty surrounding the potential implementation of this solar climate intervention strategy. We identify large differences in the aerosol mass latitudinal distributions between two recently produced climate model SAI large ensembles, despite using similar climate targets and controller algorithms, with the goal of understanding the drivers of such differences. Using a hierarchy of recently produced simulations, we identify three main contributors including: 1) the rapid adjustment of clouds and rainfall to elevated levels of carbon dioxide, 2) the associated low-frequency dynamical responses in the Atlantic Meridional Overturning Circulation, and 3) the contrasts in future climate forcing scenarios. Each uncertainty is unlikely to be significantly narrowed over the likely timeframe of a potential SAI deployment if a 1.5C target is to be met. The results thus suggest the need for significant flexibility in climate intervention deployment in order to account for these large uncertainties in the climate system response.

### Plain Language Summary

The continued high levels of anthropogenic greenhouse gas emissions increase the likelihood that key climate warming thresholds will be exceeded in the coming decades unless some form of climate intervention is implemented. It is in this context that we examine a recently proposed approach to stratospheric aerosol injection. Using two recently produced climate model experiments, we find the associated latitudinal distribution of aerosol mass to exhibit substantial uncertainty, suggesting the need for significant flexibility in the location and amount of aerosol delivery. The uncertainty's origins stem mainly from simulated climate responses to increases in carbon dioxide including rapid adjustments in clouds and rainfall, and changes in the overturning ocean circulation.

Uncertainty in future anthropogenic emissions of industrial sulfate aerosols also contribute.

## 1 Introduction

Solar climate intervention (SCI), or solar geoengineering, has been proposed as a means of reducing the adverse impacts of climate change via the artificial enhancement of Earth’s albedo. One SCI method proposed to temporarily offset anthropogenic warming and associated impacts is stratospheric aerosol injection (SAI), which involves the delivery of aerosols or precursor gases into the stratosphere. A major uncertainty surrounding the enactment of SAI is the climate system response to both continued emissions of carbon dioxide and prolonged elevated levels of stratospheric sulfate aerosols.

It is in the context of this uncertainty that the National Academies of Sciences, Engineering, and Medicine (NASEM) recently called for further research to understand various SCI approaches (NASEM, 2021) as SAI has been shown, in principle, to be a method of global climate intervention capable of achieving various temperature-based targets (Tilmes et al. 2018, MacMartin et al. 2019, Simpson et al. 2019). However, there remain large uncertainties in associated climate responses and impacts (Fasullo et al. 2018, Kravitz and MacMartin 2020) and adverse effects have been identified involving the water cycle and circulations in the troposphere, stratosphere, and ocean (Tilmes et al. 2018, Kawatani et al. 2011, Watanabe and Kawatani 2012, Fasullo et al. 2018, Xu et al. 2020, Xie et al. 2021, Sun et al. 2020, Abiodun et al. 2021, Banerjee et al. 2021 Krishnamohan and Bala 2022).

Climate models are an essential tool for exploring the potential benefits and impacts of the broad range of proposed SAI approaches. They depict the interactions between multiple processes involved in the climate response and simulate impact-relevant fields. They also provide a process-based understanding of response mechanisms and timescales. Due to the large internal variability of the climate system, the evaluation of SAI approaches often requires climate model large ensembles (Deser et al., 2012, Kay et al. 2015, Maher et al. 2021) using Earth system models (ESMs) capable of accurately representing a diverse set of processes involving stratospheric and tropospheric dynamics and chemistry, and time-varying aerosol distributions, aspects that are well-represented in only a few currently available ESMs (Franke et al. 2021).

While some recent work has found broad consistency in simulated responses to simple SAI depictions, such as solar dimming (e.g. Kravitz et al. 2021, Visioni et al. 2021), this work identifies and explores substantial climate response dependencies to a more realistic SAI representation based on explicitly resolved stratospheric aerosol injections, their evolving aerosol size distributions and burdens, their interactions with dynamical, chemical, and hydrologic processes, and related couplings between the land, atmosphere, ocean, and cryosphere (MacMartin et al. 2017, Tilmes et al. 2018, Richter et al. 2022). In this work, we explore the origin of inter-model differences and their physical bases. The

models, experiments, and methods used are described in Section 2. The spatial and temporal structure of injected aerosols and climate responses are presented and discussed in Section 3 while the broader consequences for the potential implementation of SAI, and suggestions for future work, are presented in Section 4.

## 2 Materials and Methods

### 2.1 Models

With the goal of explicitly representing the dynamical, chemical, and hydrological aspects of the climate response to SAI, this work uses versions 1 and 2 of the Community Earth System Model (CESM1, CESM2). Both versions can be run in so-called high-top and low-top atmospheric configurations. The CESM1 high-top configuration uses the Whole Atmosphere Community Climate Model, version 5 (CESM1-WACCM5, Mills et al., 2017) as its atmospheric component and the CESM2 uses WACCM6 (CESM2-WACCM6, Gettelman et al. 2019). For the atmosphere, CESM1-WACCM5 has zonal and meridional resolutions of  $0.9^\circ$  and  $1.25^\circ$ , respectively, with 70 vertical levels and a model top of 140 km. The configuration allows for a full representation of stratospheric dynamics and has extensive middle atmospheric chemistry, and is a key improvement upon earlier model generations and many current climate models (e.g., Ferraro et al., 2015). Tropospheric physics in WACCM5 are the same as in the lower top configuration, the Community Atmosphere Model version 5 (CAM5, Park et al. 2014), the atmospheric component of the CESM1 (Hurrell et al. 2013). CESM1-WACCM5 explicitly simulates sulfate aerosol concentrations and size distributions via the Modal Aerosol Module (MAM3; Mills et al., 2017). Associated responses in ozone concentrations have a beneficial impact on the stratospheric circulation and its biennial variability (Richter et al., 2017) and these have been shown to reduce the  $\text{CO}_2$ -driven midlatitude jets' poleward shift under present-day climate change (Chiodo and Polvani, 2019). Confidence in the representations of sulfate aerosol processes and their radiative effects are bolstered by the relatively close agreement that exists between simulated and observed radiative responses to the 1991 eruption of Mount Pinatubo (Mills et al., 2017). The ocean component of all models used in this study is the Parallel Ocean Program version 2 (POP2; Smith et al., 2010; Danabasoglu et al., 2012), which has uniform zonal resolution of  $1.125^\circ$ , and variable meridional resolution ranging from  $0.27^\circ$  in the tropics to  $0.64^\circ$  in the extratropical northern hemisphere. The model has 60 vertical levels with a uniform resolution of 10 m in the ocean's upper 160 m.

CESM2-WACCM6 incorporates various advances including fully interactive tropospheric chemistry and an interactive crop model. Tropospheric physics is largely the same as in the low-top configuration, the Community Atmosphere Model version 6 (CAM6) as a concerted effort was made during development of these models to use the same model tuning in the low-top and high-top configurations in order to promote inter-version comparison (Gettelman et al. 2019). CAM6 is the atmospheric component of CESM2 (Danabasoglu et al. .2020)

and uses the Cloud Layers Unified By Binormals (CLUBB; Golaz et al., 2002; Larson, 2017) unified turbulence scheme and the updated Morrison-Gottelman microphysics scheme (MG2; Gottelman and Morrison, 2015). Minor changes to POP2 are incorporated in CESM2-WACCM6 (Danabasoglu et al., 2020).

## 2.2 CESM1-WACCM5 Simulations

A summary of design characteristics for the simulations used here are given in Table 1. We use CESM1-WACCM5 SAI simulations that are a part of the Geoengineering Large Ensemble (GLENS, Tilmes et al., 2018). GLENS consists of two large ensemble of simulations: one without and one with SAI. Both ensembles use the Representative Concentration Pathway 8.5 (RCP85) emissions scenario for greenhouse gases. The baseline GLENS simulations consists of free running RCP85 simulations from 2005 through 2030 (17 members), with an additional 3 members continuing through 2100 (CESM1-WACCM5-RCP85). The second set of GLENS simulations, GLENS-SAI, utilizes strategically enacted SAI (following Kravitz et al. 2017), which consists of twenty members from 2020 to 2097 in which aerosol injections are specified by a controller algorithm (MacMartin et al. 2014, Kravitz et al. 2017) to achieve stabilization of temperature targets at their mean 2020 conditions under RCP85. The targets include near-surface air temperature’s global mean, equator-to-pole gradient, and inter-hemispheric gradient, which are all successfully stabilized in GLENS-SAI, though the equator-to-pole gradient increases slightly (by about 0.1 K from 2050 to 2070, Tilmes et al. 2018). The predefined injection latitudes for GLENS-SAI are 15° and 30° in each hemisphere and SO<sub>2</sub> is injected about 5 km above the tropopause, or approximately 25 and 23 km for the 15° and 30° sites, respectively, with an arbitrarily chosen longitude of 180° (Tilmes et al. 2018). The initialization of GLENS-SAI is made from three distinct members of the RCP85 experiment, which itself branched from distinct historical-era simulations, thus providing a diversity of initialized ocean states. GLENS has been used in a range of contexts (Fasullo et al. 2018, Simpson et al. 2019, Pinto et al., 2020, Da-Allada et al, 2020).

## 2.3 CESM2-WACCM6 Simulations

As with GLENS, we use two sets of CESM2-WACCM6 experiments. The CESM2-WACCM6 baseline simulations used are from the Coupled Model Intercomparison Project version 6 (CMIP6, Eyring et al. 2016) and the Assessing Responses and Impacts of Solar climate intervention on the Earth system with Stratospheric Aerosol Injection project ARISE-SAI, Richter et al. 2022). These include the unmitigated CMIP6 SSP585 simulations, to allow for comparison with the RCP85 experiments in GLENS (Tilmes et al. 2020). The second experiment used is the SAI ensemble, with strategically placed sulfur dioxide injection to keep the global mean temperature at  $\sim 1.5$  C over preindustrial temperatures (ARISE-SAI-1.5, Richter et al. 2022). These simulations extend from 2035 to 2069 and use the same controller algorithm and target metrics as GLENS-SAI, but for the 2020-2039 time average in the unmitigated CESM2-WACCM6 baseline simulations, in contrast to GLENS-SAI where targets are based on

the 2010 – 2030 time period. Target metrics are successfully met in ARISE-SAI-1.5 to within 0.05 K over the period 2050 to 2070 (Richter et al. 2022). The injections are again at 15° and 30 ° in both hemispheres and at an arbitrarily chosen longitude of 180°, as in GLENS-SAI, but occur lower in the stratosphere (approximately 21 km). The slight difference in injection height between GLENS-SAI and ARISE-SAI doesn’t significantly impact their efficacy however as the shortwave optical depth of the stratosphere is small relative to the troposphere. Moreover, single point injections result in strong similarity in the latitudinal structure of aerosol optical depth between CESM1 (Tilmes et al., 2017) and CESM2 (Visioni et al., 2022), with circulation differences and lifetime effects contributing to slightly greater aerosol optical depths in GLENS (Visioni et al. 2022). ARISE-SAI-1.5 simulations use the moderate Shared Socioeconomic Pathway (SSP) scenario of SSP245 for its defacto future scenario (Burgess et al., 2020), a moderate scenario where “the world follows a path in which social, economic, and technological trends do not shift markedly from historical patterns” (O’Neill et al. 2016). The temperature targets for ARISE-SAI-1.5 are based on the same regional metrics as used in GLENS-SAI and the simulations consist of a 10-member ensemble.

#### 2.4 Additional Simulations

In order to gain insight into the drivers of contrasts between the above SAI simulations, we use additional experiments. Below the stratosphere, CAM5 and CAM6 use physical representations of the climate system that are highly similar to their WACCM counterparts. Simulations using them therefore provide a means for inferring the tropospheric contribution to contrasts in our SAI experiments. For example, the ensemble mean of the CESM1 and CESM2 large ensembles (LE) provides an estimate of the future forced response (to both warming and CO<sub>2</sub> increases) by averaging across members, and through internally driven variability. Simulations used here include the 40-member CESM1-LE (Kay et al. 2015) and 100-member CESM2-LE (Rodgers et al. 2021), and a 10-member ensemble of CESM2 that makes use of CMIP5 historical and RCP85 prescribed forcing agents, (CESM2-RCP85, Forster et al. 2013). These large ensembles extend from 1850 to 2100, though for the CESM1-LE and CESM2-RCP85 only a single member spans 1850-1920. Also notable is the fact that the CESM2-LE uses SSP370 for its future scenario, rather than the SSP245 used in ARISE or the SSP585 used in future CESM2-WACCM6 simulations, and these differences complicate direct comparisons, as discussed further below. SSP370 represents the medium to high end of plausible future pathways and represents a forcing level common to several unmitigated SSP baselines

To quantify rapid adjustments to CO<sub>2</sub>, those that occur in the absence of surface warming (e.g. Tilmes et al. 2013), idealized experiments using CESM1 and CESM2 are also used in which CO<sub>2</sub> is quadrupled in both fixed sea surface temperature (SST, 4xCO<sub>2</sub>AMIP) and coupled ocean (Abrupt4xCO<sub>2</sub>) frameworks. Conversely, slow responses to warming are those that ensue in response to surface warming when CO<sub>2</sub> levels and other climate forcing agents are fixed,

and these are estimated from so-called AMIP+4K experiments where uniform SST increases of 4 K are imposed on an AMIP background state. For these sensitivity experiments, the accompanying AMIP and pre-industrial coupled experiments are used to estimate ‘control’ conditions. Together, these simulations allow for the estimation of both so-called “rapid adjustments” to  $\text{CO}_2$  and “slow responses” to warming, and these are found to provide important insight into contrasts between GLENS and ARISE. Rapid adjustments also exist for other climate forcings, such as aerosols, and in the stratosphere these effects can be significant locally (Richter et al. 2017). On planetary scales however these have been shown generally to be small relative to the adjustment to  $\text{CO}_2$  (Andrews et al., 2009; Bala et al., 2010; Samset et al., 2016; Tilmes et al., 2013).

### 3 Results

The yearly stratospheric aerosol mass injections specified in GLENS-SAI and ARISE-SAI-1.5 are shown in Figure 1, where we examine the common period of 2035 to 2069 (Table 1). The greater total emissions in GLENS-SAI than ARISE-SAI-1.5 are expected as they correspond to greater total offset  $\text{CO}_2$  concentrations. However less expected is the large disparity in the latitudinal distribution of injections, with the vast majority of GLENS-SAI aerosols injected at  $30^\circ\text{N}$  and  $30^\circ\text{S}$ , with modest injection amounts occurring at  $15^\circ\text{N}$  and negligible injection mass at  $15^\circ\text{S}$ . This contrasts starkly with ARISE-SAI-1.5, where injections occur overwhelmingly at  $15^\circ\text{S}$ , with much smaller injection amounts at  $15^\circ\text{N}$  and  $30^\circ\text{S}$ , and negligible injection mass at  $30^\circ\text{N}$ . These relative proportions and their contrasts are approximately constant over time from 2035 to 2069, suggesting that they are relatively insensitive to the associated total avoided warming or the control period used for climate targets. Rather the persistence of the distributions over time suggests the possibility of an intrinsic contrast in the climate responses between the two ensembles.

To explore the processes that may underlie the contrasts in Fig. 1, the normalized structure of warming in a range of additional simulations is examined in Figure 2. Normalized warming patterns from 2020-39 and 2050-69 in the associated unmitigated simulations (i.e. CESM1-WACCM5-RCP85 and CESM2-WACCM6-SSP585) show various features expected under anthropogenic climate change such as greater warming over land and in polar regions (Fig. 2a, b). Differences between the experiments are also clearly evident, particularly in the northern hemisphere (NH) extratropics, where warming is stronger in CESM1-WACCM5-RCP85 and a strong cooling in the North Atlantic (NATL) is evident in CESM2-WACCM6-SSP585. Differencing the normalized warming patterns (Fig. 2c) highlights systematically weaker warming in the NH in CESM2-WACCM6-SSP585 and stronger warming in the southern hemisphere (SH) subtropics, particularly in the subtropical stratocumulus cloud deck regions in the eastern ocean basins. When the analogous difference is computed between the CESM1-LE and CESM2-LE (Fig. 2d) a similar overall pattern emerges, albeit with slightly weaker magnitudes in the extratropical NH and SH. The strong similarities of patterns in Fig. 2c/d suggest a potentially dominant contribution

from tropospheric physics in CAM5 and CAM6, which as discussed earlier are shared by their WACCM counterparts. The existence of differences between Figs. 2c/d suggests a potential role for both WACCM physics and scenario contrasts between the ensembles. The role of scenario can be estimated by examining differences between CESM2-RCP85 and CESM2-LE (Fig. 2e, note the scaling used). The persisting negative differences in the NH and positive differences in the SH subtropics suggest that the contrasts between SSP370, which is the future scenario used for the CESM2-LE (Fig. 2d), and RCP85 contribute to the pattern in Fig. 2d but are not the dominant contributor to it. Given this, potential contributors to the pattern are explored further below. Also notable is the result that various features of the unmitigated warming contrast between CESM1-WACCM5-RCP85 and CESM2-WACCM6-SSP585 (Fig. 2c) are shared by the differences in SAI regional warming patterns (Fig. 2f), such as the elevated warming in the southern subtropics, and relative cooling in the NATL and NH subpolar regions, in ARISE-SAI-1.5 relative to GLENS-SAI, suggesting that these features may be intrinsic model responses.

To further explore the origin of model responses, changes in top-of-atmosphere (TOA) absorbed solar radiation (FSNT) are assessed and found to be strongly tied to patterns of warming. In unmitigated CESM1-WACCM5-RCP85 and CESM2-WACCM6-SSP585 simulations (Fig. 3a, b) normalized increases in FSNT are widespread, consistent with 21<sup>st</sup> century climate projections generally (Trenberth and Fasullo, 2009). However the inter-model difference (Fig. 3c) shows a strong spatial correlation with contrasting patterns of warming (Fig. 2c) as stronger SH subtropical warming in CESM1-WACCM5-RCP85 is accompanied by disproportionate FSNT increases while enhanced NATL cooling is coincident with FSNT decreases. When normalized patterns in the CESM1-LE and CESM2-LE are compared (Fig. 3d), a similar general pattern of FSNT differences exists, albeit slightly weaker, again suggesting the patterns to be an intrinsic feature of CAM5 and CAM6, with a potential secondary contribution from WACCM or scenario contrasts. When the CESM2-LE is compared to CESM2-RCP85 a similar but significantly weaker pattern of differences is evident (Fig. 3e, note the scaling used), suggesting a modest but detectible role for the future scenario in driving contrasts between the simulations. Unlike the temperature response under SAI, the difference pattern of FSNT change between ARISE-SAI-1.5 and GLENS-SAI is not strongly correlated with that of the unmitigated simulations and instead largely reflects the combined and complex influence of changes in clouds and SAI (Fig. 3f).

Various additional analyses provide important background for interpreting contrasts in our SAI experiments. In Fig. 3, a focus on changes in patterns of FSNT is motivated by their dominant contribution to the overall pattern of net TOA flux (Fig. S1). While changes in outgoing longwave radiation exist (Fig. S2), these can generally be viewed as responding to differences in warming, rather than driving them, as they are positively correlated to temperature anomalies and thus offset, in many cases, changes in FSNT. Understanding the origin of spatial patterns and interhemispheric FSNT gradients in unmitigated simula-

tions is therefore critical to anticipating the latitudinal distribution of injection amounts under SAI.

In this context the 4xCO<sub>2</sub>AMIP and Abrupt4xCO<sub>2</sub> simulations provide important insight as they demonstrate that responses in shortwave radiation and clouds to elevated levels of CO<sub>2</sub> (i.e. rapid adjustments) also differ considerably between CESM1 and CESM2 in a way that is consistent with the need for greater NH mitigation in the GLENS-SAI experiment. For example, in CESM1 there is a strong hemispheric gradient in FSNT rapid adjustments (Fig. 4) such that the NH absorbs 2.4 W m<sup>-2</sup> more energy than the SH in response to a CO<sub>2</sub> quadrupling. In contrast, in CESM2 the response is relatively symmetric between hemispheres with an imbalance of only 0.4 W m<sup>-2</sup>, with strong warming contributions evident in the SH subtropics, as also identified as being key in Figs. 2, 3. These experiments therefore show that rapid adjustments are likely an important contributor to the patterns in unmitigated simulations and to injection mass contrasts between GLENS-SAI and ARISE-SAI-1.5, as CO<sub>2</sub> levels continue to increase in these simulations. Moreover, the radiation contrasts can be linked to rapid adjustments in clouds, with reductions in cloud amount in the southern hemisphere subtropics being closely tied to associated increases in FSNT. It is also notable that the hemispheric contrasts in the slow responses to warming also contrast significantly between models, with the pattern in CESM1 being hemispherically asymmetric and offsetting rapid adjustments, and the pattern in CESM2 being approximately symmetric (Fig. S4). While regional features are more difficult to interpret in fully coupled simulations due to the presence of coupled internal variability, it is noteworthy that disproportionate FSNT increases in the NH also emerge in the early years of Abrupt4xCO<sub>2</sub> experiments and these are sustained for several decades. Together these findings highlight the need to understand the sensitivity of the climate response directly to CO<sub>2</sub> if uncertainties in the implementation of SAI are to be reduced.

Contrasting warming patterns in the Atlantic Ocean are also suggestive of the involvement of an additional important component of the energy budget, the Atlantic Meridional Overturning Circulation (AMOC), which transports heat northward in the Atlantic and redistributes ocean mass, nutrients, salinity, and energy globally (Zhang et al. 2019). Differences between the response in AMOC in our experiments are explored in Figure 5. Changes in the strength of the leading mode of AMOC (Fig. 5a) contrast considerably across the experiments. In GLENS-SAI, the intensity of AMOC increases and this drives an associated enhanced northward transport of heat into the NATL (Fasullo et al. 2018). The strengthening contrasts however with all other simulations considered here (Fig. 5a) and with unmitigated climate projections generally (Zhang et al. 2019, Xie et al. 2021), where AMOC typically weakens during the 21<sup>st</sup> century. A similar decrease in intensity is evident between ARISE-SAI-1.5 and the unmitigated CESM1-WACCM5-RCP85 and CESM2-WACCM-SSP585. A key driver of AMOC's leading mode is deep water formation in the NATL and in this region simulation of ocean density and salinity also differ substantially between the various experiments. In GLENS-SAI, the subpolar NATL becomes denser

and more saline (Fig 5b, 5c) while the subtropical north Atlantic Ocean becomes less dense. These changes accompany increases in evaporation and a net negative surface freshwater flux, which enhances salinity and density (Fasullo et al. 2018). In ARISE-SAI-1.5 the situation is reversed, with the subpolar NATL becoming substantially less dense and fresher, with associated reductions in evaporation (not shown). In ARISE-SAI-1.5, density reductions are evident in the Atlantic at all latitudes below 200 to 500 m due to warming (not shown) and salinity increases are evident south of 40N, patterns that contrast markedly with GLENS-SAI. Causal connections between salinity, density, and AMOC intensity can be complex however and will be discussed further below.

The sensitivity of AMOC to  $\text{CO}_2$  and SAI also exists as a key uncertainty. Diagnosing individual drivers of AMOC in fully coupled simulations is extremely challenging given the diversity of thermal, saline, and dynamical processes that drive its changes (Zhang et al. 2019) and achieving a full understanding of contrasts between GLENS-SAI and ARISE-SAI-1.5 is left for future work. However, various changes are simulated that are consistent with having an influence and these include the modulation of salinity and density in the NATL (Zhang et al. 2022), as in ARISE-SAI-1.5 a widespread freshening and decrease in density are simulated, in contrast to salinity and density increases simulated in GLENS-SAI (Fig. S6). A similar salinity contrast is also simulated in future unmitigated simulations using CESM2-WACCM-SSP585 and CESM1-WACCM5-RCP85, and in the CESM2-LE and CESM1-LE, suggesting that the contrast is intrinsic, at least in part, to CAM5 and CAM6 structural contrasts (Fig. S6). This possibility is supported further by rapid adjustments in precipitation to  $\text{CO}_2$ , as CESM2 simulates systematically weaker reductions in precipitation in the northern extratropics than does CESM1 (Fig. 6), both over the Atlantic Ocean and over much of northern extratropical land where river discharge influences ocean salinity. While neither model simulates changes in rainfall that on their own would weaken AMOC, the potential for negative surface freshwater contributions to offset the elevated buoyancy driven by warming is suggested to differ considerably. More precise attribution of AMOC changes and their contrasts between experiments likely requires additional targeted experiments, the results here point to a potentially important role for rapid adjustments in the water cycle.

Lastly, a role for the future climate scenario in influencing the latitudinal distribution of SAI injection mass is suggested by the differences between CESM2-LE and CESM2-RCP85 warming and radiation patterns, given the stronger NH warming and FSNT increases east of important sulfate emissions regions in Asia in simulations using RCP85 (negative differences in Figs. 2e, 3e, S1e, S2e). This hypothesis can be explored by examining changes in atmospheric sulfate burdens (Fig. 7), which differ significantly through the 2030-70 period between the experiments used. As discussed previously, comparison across these experiments is complicated by the differences in the scenarios used in each. However, the fact that differences in the sulfate distributions across experiments are both significant and correspond directly to simulated features in radiation and tem-

perature suggests a role as a mediating effect on SAI experiments. In general, simulations that use RCP85 emissions show stronger reductions in burdens than those that use SSP370 (Fig. 7d, e) or SSP585 (Fig. 7c). Given the strong cooling associated with the burdens via their impact on clouds, these differences constitute an anomalous NH warming contribution in the 21<sup>st</sup> C for RCP85-based experiments (Fig. 7c-e) that thus require additional NH mitigation (Fig. 7f).

#### 4 Discussion and Conclusions

The analysis of our climate intervention and complementary experiments highlights a fundamental and perhaps underappreciated contributor to uncertainties surrounding SAI, the rapid adjustments of the climate system to CO<sub>2</sub>. Such adjustments include both the responses of patterns in cloud fields, which drive radiation contrasts between hemispheres, and precipitation, which can influence upper ocean salinity, density, and associated ocean circulations and energy flows. As shown here, the simulation of rapid adjustments can vary considerably across models and resolving these inter-model discrepancies is thus critical in order to better constrain the design parameters of SAI if implemented in nature. Uncertainties in future scenarios must also be reduced in order to winnow the spread across SAI simulations, and progress along this front has been made in recent years with the identification of biases in prescribed CMIP6 emissions (e.g. Paulot et al. 2018, Wang et al. 2021). Notably however, the climate response uncertainty associated with prescribed sulfate emissions is magnified by the broad range with which aerosol indirect effects on clouds as represented across climate models. The inference from the SAI simulations explored here is that the latitude of SAI injections will depend explicitly on ambient anthropogenic emissions of sulfate aerosols and formulation of an SAI strategy should therefore be accompanied by well-defined industrial emissions targets.

There are also important limits on the results shown here. First, they are based on only two climate models, and in many respects these models share physics that is central to the representation of SAI. A broader consideration of structural model uncertainty is therefore warranted and it is likely that key sources of uncertainty, such as cloud-aerosol interactions, are not well-estimated in contrasts between our experiments. A need therefore exists for a broader multi-model effort to realistically depict SAI and its uncertainties and to coordinate associated model development efforts. Notably a vast majority of climate models currently cannot represent the diversity of associated processes and fields simulated in WACCM. Observational efforts to monitor relevant fields and guide model development activities are also crucial if the inherent risks and uncertainties of SAI are to be understood, quantified, and reduced to a point where SCI might become a promising risk-mitigation measure.

#### Acknowledgments

This material is based upon work supported by the National Center for Atmospheric Research (NCAR), which is a major facility sponsored by the National

Science Foundation (NSF) under Cooperative Agreement 1852977 and by SilverLining through its Safe Climate Research Initiative. The CESM project is supported primarily by the NSF. Computing and data storage resources, including the Cheyenne supercomputer (doi:10.5065/D6RX99HX), were provided by the Computational and Information Systems Laboratory (CISL) at NCAR. We thank all the scientists, software engineers, and administrators who contributed to the development of CESM2. JF was also supported by NASA Awards 80NSSC17K0565 and 80NSSC22K0046.

### **Availability Statement**

All GLENS-SAI and CESM1-WACCM5-RCP85 simulations are available to the community via the Earth System Grid (see information at [www.cesm.ucar.edu/projects/community-projects/GLENS/](http://www.cesm.ucar.edu/projects/community-projects/GLENS/)). Output from the CESM1-LE, CESM2-LE, CESM2-RCP85, CESM2-WACCM6-SSP585, simulations and ARISE-SAI-1.5 simulations is freely available the NCAR Climate Data Gateway at <https://doi.org/10.26024/0cs0-ev98> and <https://doi.org/10.5065/9kcn-9y79> respectively. CMIP6 data including CESM2-WACCM6-SSP585, 4xCO2AMIP, and 4xAbruptCO<sub>2</sub> simulations are available online (<https://esgf-node.llnl.gov/projects/cmip6/>).

### **Author Contributions**

Conceptualization: J. T. Fasullo, J. H. Richter

Data curation: J. T. Fasullo, J. H. Richter

Formal analysis: J. T. Fasullo

Funding acquisition: J. H. Richter

Methodology: J. T. Fasullo, J. H. Richter

### **References**

- Abiodun, B. J., Odoulami, R. C., Sawadogo, W., Oloniyo, O. A., Abatan, A. A., New, M., ... & MacMartin, D. G. (2021), Potential impacts of stratospheric aerosol injection on drought risk managements over major river basins in Africa. *Climatic Change*, 169(3), 1-19, <https://doi.org/10.1007/s10584-021-03268-w>.
- Andrews, T., Forster, P. M., & Gregory, J. M. (2009). A surface energy perspective on climate change. *Journal of Climate*, 22(10), 2557–2570. <https://doi.org/10.1175/2008JCLI2759.1>
- Bala, G., Caldeira, K., & Nemani, R. (2010). Fast versus slow response in climate change: Implications for the global hydrological cycle. *Climate Dynamics*, 35(2-3), 423–434. <https://doi.org/10.1007/s00382-009-0583-y>.
- Banerjee, A., Butler, A. H., Polvani, L. M., Robock, A., Simpson, I. R., & Sun, L. (2021), Robust winter warming over Eurasia under stratospheric sulfate

- geoengineering—the role of stratospheric dynamics. *Atmospheric Chemistry and Physics*, 21(9), 6985-6997, <https://doi.org/10.5194/acp-21-6985-2021>.
- Burgess, M. G., J. Ritchie, J. Shapland & Pielke R. Jr. (2021), IPCC baseline scenarios have over-projected CO2 emissions and economic growth. *Env. Res. Lett.*, 16, 014016, <https://doi.org/10.1088/1748-9326/abcdd2>.
- Chiodo, G., & Polvani, L. M. (2019), The Response of the Ozone Layer to Quadrupled CO 2 Concentrations: Implications for Climate. *Journal of climate*, 32(22), 7629-7642, <https://doi.org/10.1175/JCLI-D-19-0086.1>.
- Da-Allada, C. Y., Baloitcha, E., Alamou, E. A., Awo, F. M., Bonou, F., Pomalagni, Y., ... & Irvine, P. J. (2020), Changes in west African summer monsoon precipitation under stratospheric aerosol geoengineering. *Earth's Future*, 8(7), <https://doi.org/10.1029/2020EF001595>.
- Danabasoglu, G., Bates, S. C., Briegleb, B. P., Jayne, S. R., Jochum, M., Large, W. G., ... & Yeager, S. G. (2012). The CCSM4 ocean component. *Journal of Climate*, 25(5), 1361-1389, <https://doi.org/10.1175/JCLI-D-11-00091.1>.
- Danabasoglu, G., Lamarque, J. F., Bacmeister, J., Bailey, D. A., DuVivier, A. K., Edwards, J., ... & Strand, W. G. (2020), The community earth system model version 2 (CESM2). *Journal of Advances in Modeling Earth Systems*, 12(2), <https://doi.org/10.1029/2019MS001916>.
- Deser, C., Phillips, A., Bourdette, V., & Teng, H. (2012), Uncertainty in climate change projections: the role of internal variability. *Climate dynamics*, 38(3), 527-546, <https://doi.org/10.1007/s00382-010-0977-x>.
- Eyring, V., Bony, S., Meehl, G. A., Senior, C. A., Stevens, B., Stouffer, R. J., & Taylor, K. E. (2016). Overview of the Coupled Model Intercomparison Project Phase 6 (CMIP6) experimental design and organization. *Geoscientific Model Development*, 9(5), 1937-1958, <https://doi.org/10.5194/gmd-9-1937-2016>.
- Fasullo, J. T., Tilmes, S., Richter, J. H., Kravitz, B., MacMartin, D. G., Mills, M. J., & Simpson, I. R. (2018), Persistent polar ocean warming in a strategically geoengineered climate. *Nature Geoscience*, 11(12), 910-914.
- Ferraro, A. J., & Griffiths, H. G. (2016), Quantifying the temperature-independent effect of stratospheric aerosol geoengineering on global-mean precipitation in a multi-model ensemble. *Environmental Research Letters*, 11(3), <https://doi.org/10.1088/1748-9326/11/3/034012>.
- Forster, P. M., Andrews, T., Good, P., Gregory, J. M., Jackson, L. S., & Zelinka, M. (2013), Evaluating adjusted forcing and model spread for historical and future scenarios in the CMIP5 generation of climate models. *Journal of Geophysical Research: Atmospheres*, 118(3), 1139-1150, <https://doi.org/10.1002/jgrd.50174>
- Franke, H., Niemeier, U., & Visioni, D. (2021), Differences in the quasi-biennial oscillation response to stratospheric aerosol modification depending on injection

strategy and species. *Atmospheric Chemistry and Physics*, 21(11), 8615-8635, <https://doi.org/10.5194/acp-21-8615-2021>.

Gettelman, A., Mills, M. J., Kinnison, D. E., Garcia, R. R., Smith, A. K., Marsh, D. R., ... & Randel, W. J. (2019). The whole atmosphere community climate model version 6 (WACCM6). *Journal of Geophysical Research: Atmospheres*, 124(23), 12380-12403, 10.1029/2019JD030943.

Golaz, J.-C., Larson, V. E., & Cotton, W. R. (2002). A PDF-based model for boundary layer clouds. Part I: Method and model description. *Journal of the Atmospheric Sciences*, 59, 3540-3551, [https://doi.org/10.1175/1520-0469\(2002\)059%3c3540:APBMFB%3e2.0.CO;2](https://doi.org/10.1175/1520-0469(2002)059%3c3540:APBMFB%3e2.0.CO;2).

Hurrell, J. W., Holland, M. M., Gent, P. R., Ghan, S., Kay, J. E., Kushner, P. J., ... & Marshall, S. (2013). The community earth system model: a framework for collaborative research. *Bulletin of the American Meteorological Society*, 94(9), 1339-1360, <https://doi.org/10.1175/BAMS-D-12-00121.1>.

Kawatani, Y., Hamilton, K., & Watanabe, S. (2011). The quasi-biennial oscillation in a double CO<sub>2</sub> climate. *Journal of the Atmospheric Sciences*, 68(2), 265-283, <https://doi.org/10.1175/2010JAS3623.1>.

Kay, J. E., Deser, C., Phillips, A., Mai, A., Hannay, C., Strand, G., ... & Vertenstein, M. (2015). The Community Earth System Model (CESM) large ensemble project: A community resource for studying climate change in the presence of internal climate variability. *Bulletin of the American Meteorological Society*, 96(8), 1333-1349, <https://doi.org/>.

Jackson, L. C., Biastoch, A., Buckley, M. W., Desbruyères, D. G., Frajka-Williams, E., Moat, B., & Robson, J. (2022). The evolution of the North Atlantic Meridional Overturning Circulation since 1980. *Nature Reviews Earth & Environment*, 1-14, <https://doi.org/10.1038/s43017-022-00263-2>.

Jones, A., Haywood, J. M., Jones, A. C., Tilmes, S., Kravitz, B., & Robock, A. (2021). North Atlantic Oscillation response in GeoMIP experiments G6solar and G6sulfur: why detailed modelling is needed for understanding regional implications of solar radiation management. *Atmospheric Chemistry and Physics*, 21(2), 1287-1304, <https://doi.org/10.5194/acp-21-1287-2021>.

Kravitz, B., MacMartin, D. G., Vioni, D., Boucher, O., Cole, J. N., Haywood, J., ... & Tilmes, S. (2021). Comparing different generations of idealized solar geoengineering simulations in the Geoengineering Model Intercomparison Project (GeoMIP). *Atmospheric Chemistry and Physics*, 21(6), 4231-4247, <https://doi.org/10.5194/acp-21-4231-2021>.

Kravitz, B., & MacMartin, D. G. (2020). Uncertainty and the basis for confidence in solar geoengineering research. *Nature Reviews Earth & Environment*, 1(1), 64-75, <https://doi.org/10.1038/s43017-019-0004-7>.

Krishnamohan, K. S., & Bala, G. (2022). Sensitivity of tropical monsoon precipitation to the latitude of stratospheric aerosol injections. *Climate Dynamics*,

1-18, <https://doi.org/10.1007/s00382-021-06121-z>.

Larson, V. E., (2017). CLUBB-SILHS: A parameterization of subgrid variability in the atmosphere. arXiv:1711.03675v2 [physics.ao-ph].

MacMartin, D. G., Kravitz, B., Tilmes, S., Richter, J. H., Mills, M. J., Lamarque, J. F., ... & Vitt, F. (2017). The climate response to stratospheric aerosol geoengineering can be tailored using multiple injection locations. *Journal of Geophysical Research: Atmospheres*, *122*(23), 12-574, <https://doi.org/10.1002/2017JD026868>.

MacMartin, D. G., Wang, W., Kravitz, B., Tilmes, S., Richter, J. H., & Mills, M. J. (2019), Timescale for detecting the climate response to stratospheric aerosol geoengineering. *Journal of Geophysical Research: Atmospheres*, *124*, 1233–1247. <https://doi.org/10.1029/2018JD028906>.

Maher, N., Milinski, S., & Ludwig, R. (2021). Large ensemble climate model simulations: introduction, overview, and future prospects for utilising multiple types of large ensemble. *Earth System Dynamics*, *12*(2), 401-418, <https://doi.org/10.5194/esd-12-401-2021>.

Mills, M. J., Richter, J. H., Tilmes, S., Kravitz, B., MacMartin, D. G., Glanville, A. A., Tribbia J. T, Lamarque J-F., Vitt F., Schmidt A., Gettelman A., Hannay C., Bacmeister J. T., and Kinnison, D. E. (2017), Radiative and chemical response to interactive stratospheric sulfate aerosols in fully coupled CESM1(WACCM). *Journal of Geophysical Research: Atmospheres*, *122*, 13,061– 13,078, <https://doi.org/10.1002/2017JD027006>.

National Academies of Sciences, Engineering, and Medicine. Reflecting Sunlight: Recommendations for Solar Geoengineering Research and Research Governance. Washington, DC: *The National Academies Press.*, <https://doi.org/10.17226/25762>, 2021.

Park, S., Bretherton, C. S., & Rasch, P. J. (2014), Integrating cloud processes in the Community Atmosphere Model, version 5. *Journal of Climate*, *27*(18), 6821-6856, <https://doi.org/10.1175/JCLI-D-14-00087.1>.

O'Neill, B. C., Tebaldi, C., Van Vuuren, D. P., Eyring, V., Friedlingstein, P., Hurtt, G., Knutti R., Kriegler E., Lamarque J-F., Lowe J., Meehl G. A., Moss R., Riahi K., and Sanderson B. M., (2016) The Scenario Model Intercomparison Project (ScenarioMIP) for CMIP6. *Geoscientific Model Development*, *9*(9), 3461–3482, <https://doi.org/10.5194/gmd-9-3461-2016>.

Park, S., Bretherton, C. S., & Rasch, P. J. (2014). Integrating cloud processes in the Community Atmosphere Model, version 5. *Journal of Climate*, *27*(18), 6821-6856, <https://doi.org/10.1175/JCLI-D-14-00087.1>.

Paulot, F., Paynter, D., Ginoux, P., Naik, V., & Horowitz, L. W. (2018). Changes in the aerosol direct radiative forcing from 2001 to 2015: observational constraints and regional mechanisms. *Atmospheric Chemistry and Physics*, *18*(17), 13265-13281, <https://doi.org/10.5194/acp-18-13265-2018>.

Pinto, I., Jack, C., Lennard, C., Tilmes, S., & Odoulami, R. C. (2020), Africa's climate response to solar radiation management with stratospheric aerosol. *Geophysical Research Letters*, 47(2), e2019GL086047, <https://doi.org/10.1029/2019GL086047>.

Richter, J. H., Tilmes, S., Mills, M. J., Tribbia, J., Kravitz, B., MacMartin, D. G., Vitt, F., and Lamarque J-F. (2017), Stratospheric dynamical response and ozone feedbacks in the presence of SO<sub>2</sub> injections. *Journal of Geophysical Research: Atmospheres*, 122, 12,557–12,573, <https://doi.org/10.1002/2017JD026912>.

Richter, J., D Visoni , D G. MacMartin , D A. Bailey , N. Rosenbloom , W. R. Lee , M. Tye , & Lamarque, J-F (2022), ARISE Assessing Responses and Impacts of Solar climate intervention on the Earth system with stratospheric aerosol injection (ARISE-SAI), *Geoscientific Model Development.*, submitted.

Rodgers, K. B., Lee, S. S., Rosenbloom, N., Timmermann, A., Danabasoglu, G., Deser, C., ... & Yeager, S. G. (2021), Ubiquity of human-induced changes in climate variability. *Earth System Dynamics*, 12(4), 1393-1411, <https://doi.org/10.5194/esd-12-1393-2021>.

Samset, B. H., Myhre, G., Forster, P. M., Hodnebrog, Ø., Andrews, T., Faluvegi, G., et al. (2016). Fast and slow precipitation responses to individual climate forcings: A PDRMIP multimodel study. *Geophysical Research Letters*, 43, 2782–2791. <https://doi.org/10.1002/2016GL068064>.

2016GL068064.

Simpson, I. R., Tilmes, S., Richter, J. H., Kravitz, B., MacMartin, D. G., Mills, M. J., Fasullo J. T., and Pendergrass A. G. (2019), The regional hydroclimate response to stratospheric sulfate geoengineering and the role of stratospheric heating. *Journal of Geophysical Research: Atmospheres*, 124, 12587–12616, <https://doi.org/10.1029/2019JD031093>.

Smith, W., & Wagner, G. (2018), Stratospheric aerosol injection tactics and costs in the first 15 years of deployment. *Environmental Research Letters*, 13(12), 124001, <https://doi.org/10.1088/1748-9326/aae98d>.

Smith, R., Jones P., Briegleb B., Bryan F., Danabasoglu G., Dennis J., Dukowicz J., Eden C., Fox-Kemper B., Gent P., Hecht M., Jayne S., Jochum M., Large W., Lindsay K., Maltrud M., Norton N., Peacock S., Vertenstein M., Year S. (2010), The Parallel Ocean Program (POP) reference manual, Ocean component of the Community Climate System Model (CCSM), LANL Technical Report, LAUR-10-01853, 141 pp.

Sun, W., Wang, B., Chen, D., Gao, C., Lu, G., & Liu, J. (2020), Global monsoon response to tropical and Arctic stratospheric aerosol injection. *Climate Dynamics*, 55(7), 2107-2121, <https://doi.org/10.1007/s00382-020-05371-7>.

Tilmes, S., Fasullo, J., Lamarque, J. F., Marsh, D. R., Mills, M., Alterskjær, K., ... & Watanabe, S. (2013). The hydrological impact of geoengineering

in the Geoengineering Model Intercomparison Project (GeoMIP). *Journal of Geophysical Research: Atmospheres*, 118(19), 11-036, doi: 10.1002/jgrd.50868.

Tilmes, S., Richter, J. H., Kravitz, B., MacMartin, D. G., Mills, M. J., Simpson, I. R., ... & Ghosh, S. (2018), CESM1 (WACCM) stratospheric aerosol geoengineering large ensemble project. *Bulletin of the American Meteorological Society*, 99(11), 2361-2371, <https://doi.org/10.1175/BAMS-D-17-0267.1>.

Tilmes, S., MacMartin, D. G., Lenaerts, J., Van Kampenhout, L., Muntjewerf, L., Xia, L., ... & Robock, A. (2020), Reaching 1.5 and 2.0 C global surface temperature targets using stratospheric aerosol geoengineering. *Earth System Dynamics*, 11(3), 579-601, <https://doi.org/10.5194/esd-11-579-2020>.

Visioni, D., MacMartin, D. G., Kravitz, B., Boucher, O., Jones, A., Lorton, T., ... & Tilmes, S. (2021), Identifying the sources of uncertainty in climate model simulations of solar radiation modification with the G6sulfur and G6solar Geoengineering Model Intercomparison Project (GeoMIP) simulations. *Atmospheric Chemistry and Physics*, 21(13), 10039-10063, <https://doi.org/10.5194/acp-21-10039-2021>.

Visioni, D., Bednarz, E. M., Lee, W. R., Kravitz, B., Jones, A., Haywood, J. M., and MacMartin, D. G.: Climate response to off-equatorial stratospheric sulfur injections in three Earth System Models - Part 1: experimental protocols and surface changes, EGUsphere, <https://doi.org/10.5194/egusphere-2022-401>, 2022.

Wang, Z., Lin, L., Xu, Y., Che, H., Zhang, X., Zhang, H., ... & Xie, B. (2021). Incorrect Asian aerosols affecting the attribution and projection of regional climate change in CMIP6 models. *NPJ Climate and Atmospheric Science*, 4(1), 1-8, <https://doi.org/10.1038/s41612-020-00159-2>.

Xie, M., Moore, J. C., Zhao, L., Wolovick, M., & Muri, H. (2021), Impacts of three types of solar geoengineering on the North Atlantic Meridional Overturning Circulation. *Atmospheric Chemistry and Physics Discussions*, 1-28, <https://doi.org/10.5194/acp-2021-877>.

Xu, Y., Lin, L., Tilmes, S., Dagon, K., Xia, L., Diao, C., ... & Burnell, L. (2020), Climate engineering to mitigate the projected 21st-century terrestrial drying of the Americas: Carbon Capture vs. Sulfur Injection. *Earth System Dynamics*, <https://doi.org/10.5194/esd-2020-2>.

Zhang, R. R. Sutton, G. Danabasoglu, Y.-O. Kwon, R. Marsh, S. G. Yeager, D. E. Amrhein, C. M. Little, (2019), A review of the role of the Atlantic meridional overturning circulation in Atlantic multidecadal variability and associated climate impacts. *Rev. Geophys.* **57**, 316-375 (2019), <https://doi.org/10.1029/2019RG000644>.

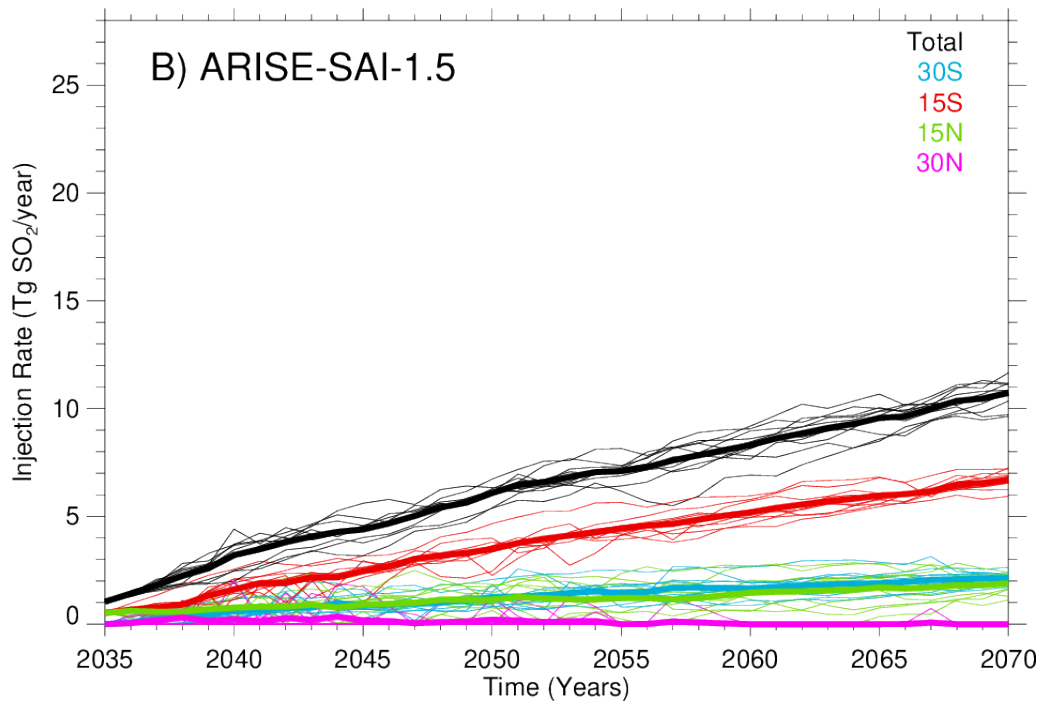
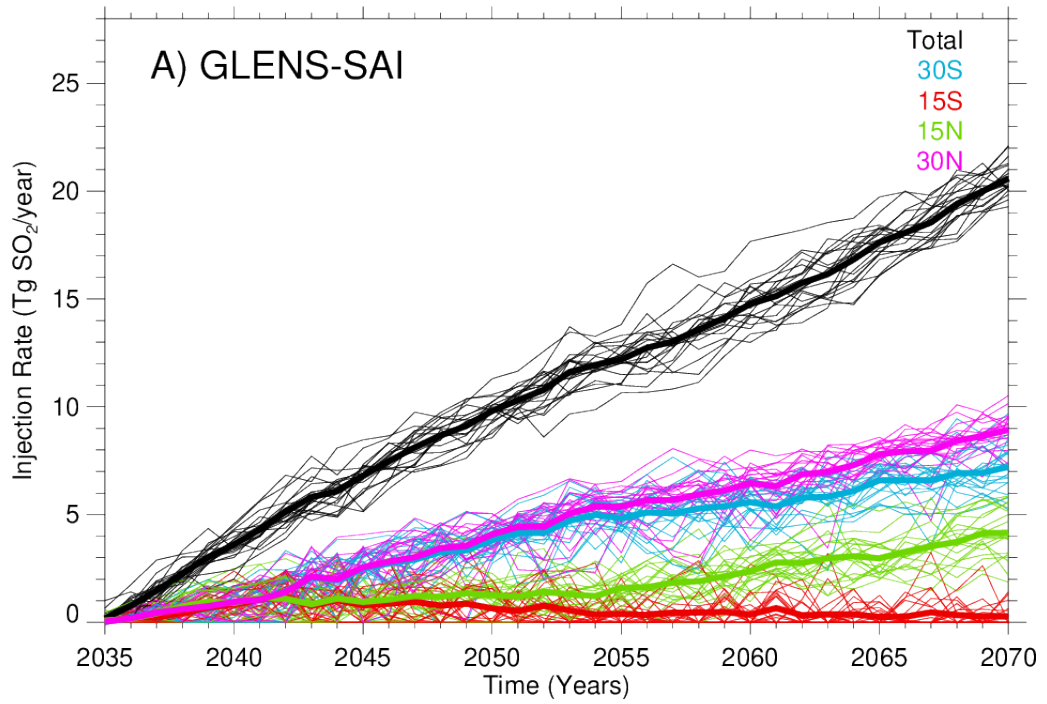
Zhang, Q., Chang, P., Yeager, S. G., Danabasoglu, G., & Zhang, S. (2022), Role of sea-surface salinity in simulating historical decadal variations of Atlantic

meridional overturning circulation in a coupled climate model. *Geophysical Research Letters*, 49, e2021GL096922. <https://doi.org/10.1029/2021GL096922>.

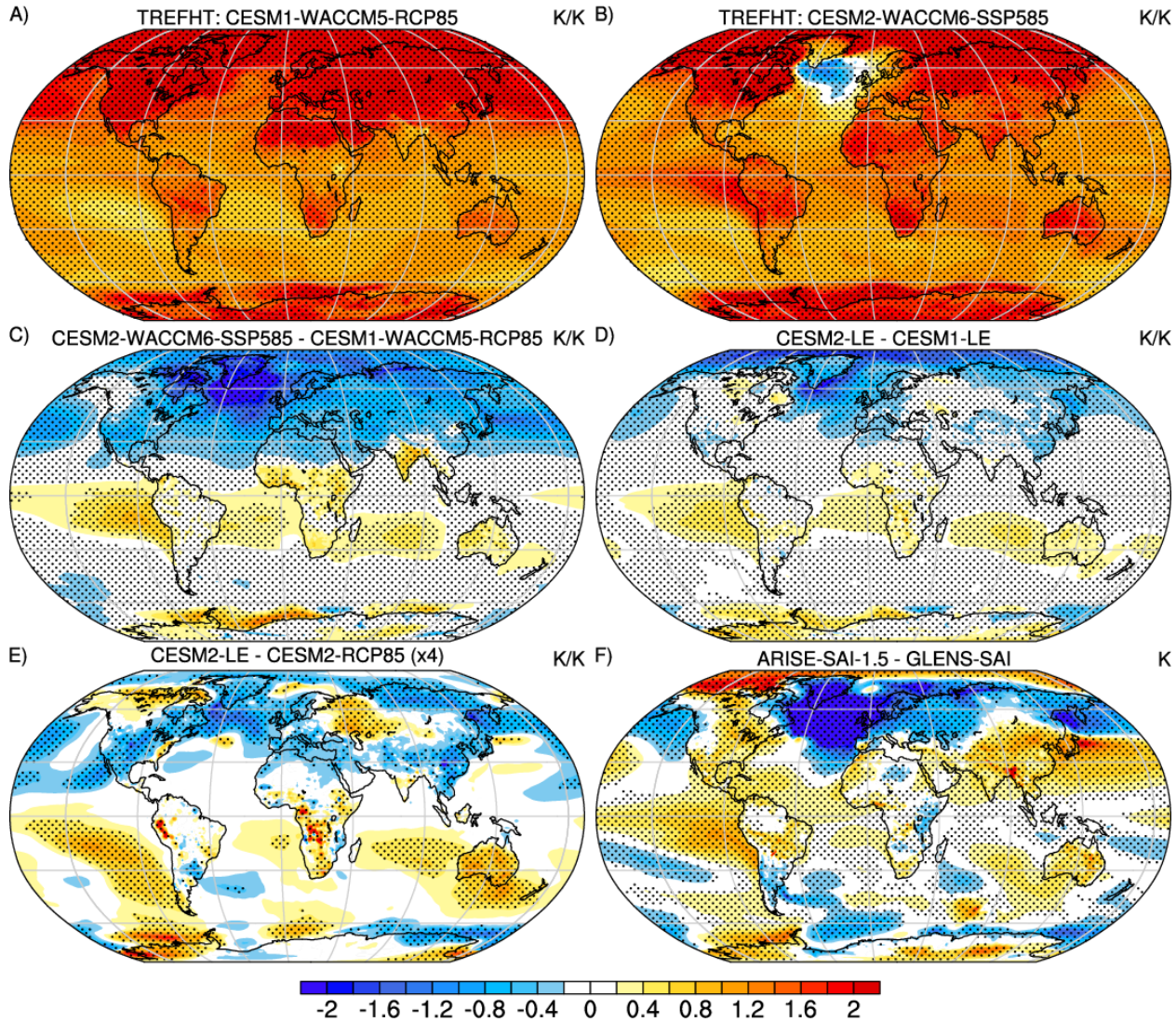
Zhao, M., Cao, L., Bala, G., & Duan, L. (2021), Climate response to latitudinal and altitudinal distribution of stratospheric sulfate aerosols. *Journal of Geophysical Research: Atmospheres*, 126, e2021JD035379. <https://doi.org/10.1029/2021JD035379>

Table 1. Climate model experiments used in this study and their design characteristics.

Ensemble Name	Lateral Resolution	Vertical Levels	# mem	Time Span	Future Scenario
CESM1-WACCM5-RCP85	0.9°x1.25°	70	20 (3*)	2006-2030 (2099)	RCP85
GLENS-SAI	0.9°x1.25°	70	20	2020-2097	RCP85+SAI
CESM2-WACCM6-SSP585	0.9°x1.25°	70	5		SSP585
ARISE-SAI-1.5	0.9°x1.25°	70	10	2035-2069	SSP245+SAI
CESM1-LE	0.9°x1.25°	30	40	1920-2100	RCP85
CESM2-LE	0.9°x1.25°	32	50	1850-2100	SSP370
CESM2-RCP85	0.9°x1.25°	32	10	1920-2100	RCP85
CESM1-AMIP	0.9°x1.25°	30	1	1979-2005	N/A
CESM1-4xCO2AMIP	0.9°x1.25°	30	1	1979-2005	N/A
CESM2-AMIP	0.9°x1.25°	32	1	1979-2014	N/A
CESM2-4xCO2AMIP	0.9°x1.25°	32	1	1979-2014	N/A
CESM2-AMIP+4K	0.9°x1.25°	32	1	1979-2014	N/A
CESM1-PI	0.9°x1.25°	30	1	0-1800	N/A
CESM2-PI	0.9°x1.25°	30	1	0-2000	N/A
CESM1-Abrupt4xCO2	0.9°x1.25°	32	1	0-150	N/A
CESM2-Abrupt4xCO2	0.9°x1.25°	32	1	0-150	N/A



**Figure 1.** Evolution of yearly sulfur dioxide injections ( $\text{Tg SO}_2 \text{ yr}^{-1}$ ) over time at the four injection latitudes for (a) GLENS-SAI and (b) ARISE-SAI-1.5 from 2035 to 2070.



**Figure 2.** Normalized response in near surface air temperature (TREFHT) estimated from the change between 2020-39 and 2050-69 per degree global warming for unmitigated (a) CESM1-WACCM5-RCP85 and (b) CESM2-WACCM6-SSP585 simulations, and (c) their difference (b-a). Also shown is (d) the analogous difference for the CESM1-LE and CESM2-LE and (e) the CESM2-RCP85 and CESM2-LE (scaled by 4). The difference between the geoengineered climate states in ARISE-SAI-1.5 and GLENS-SAI is shown in (f). Units for all panels

are  $\text{K K}^{-1}$ , except in (f) where units are  $\text{W m}^{-2}$ , and stippled regions indicate differences that exceed twice the ensemble standard error.

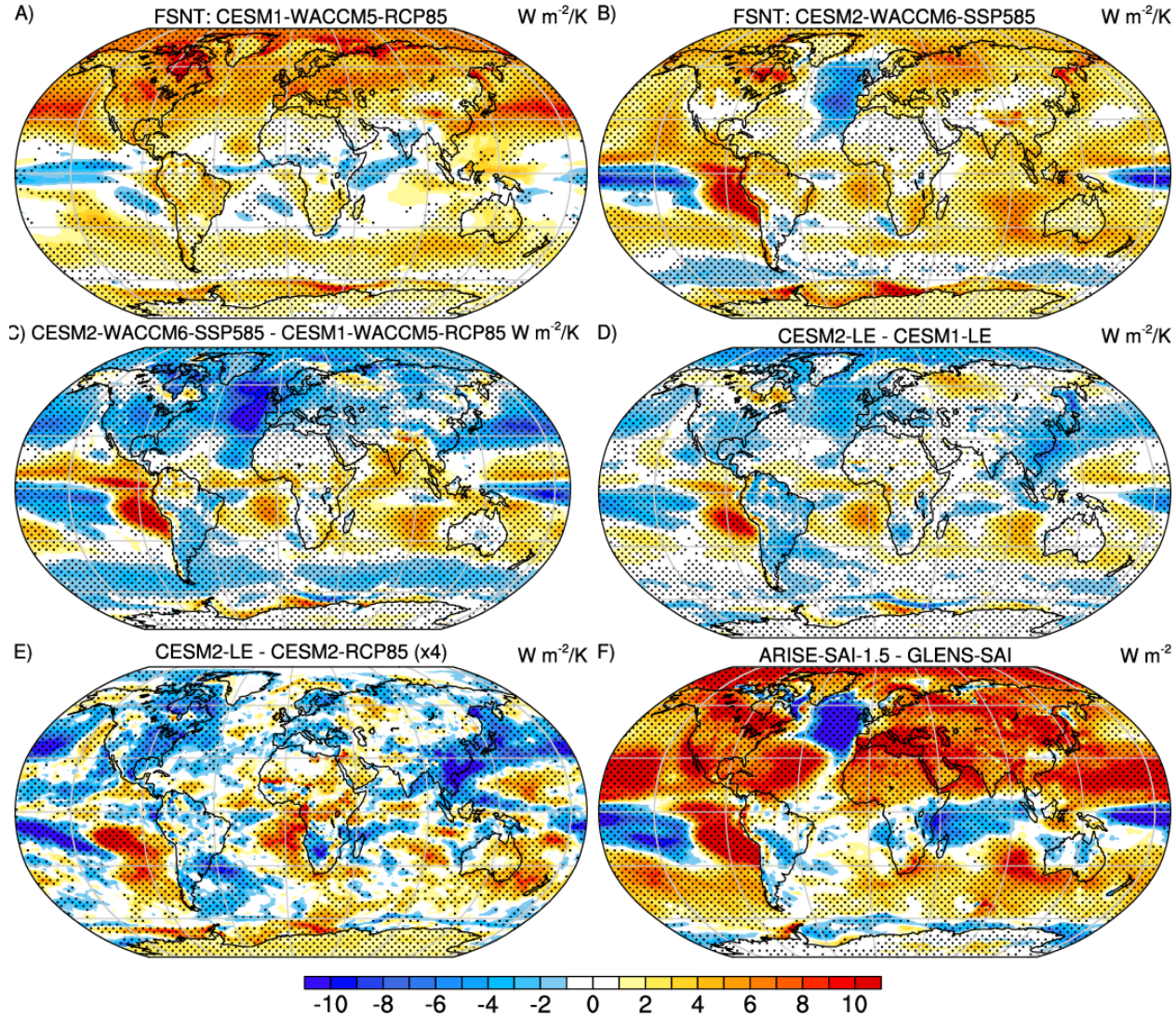
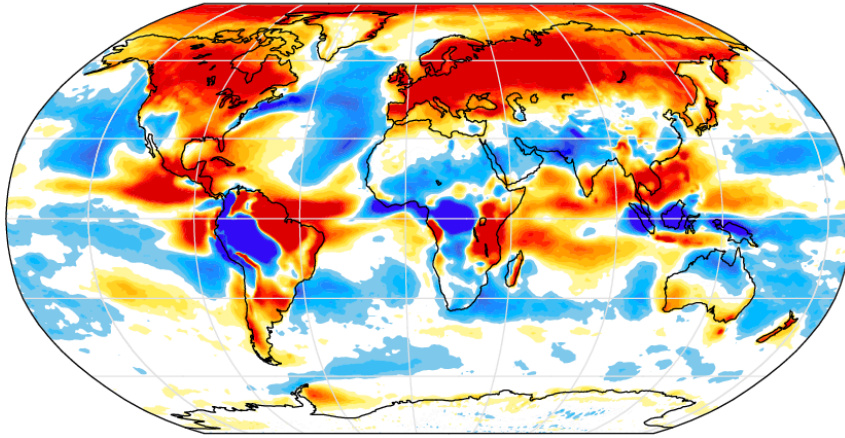


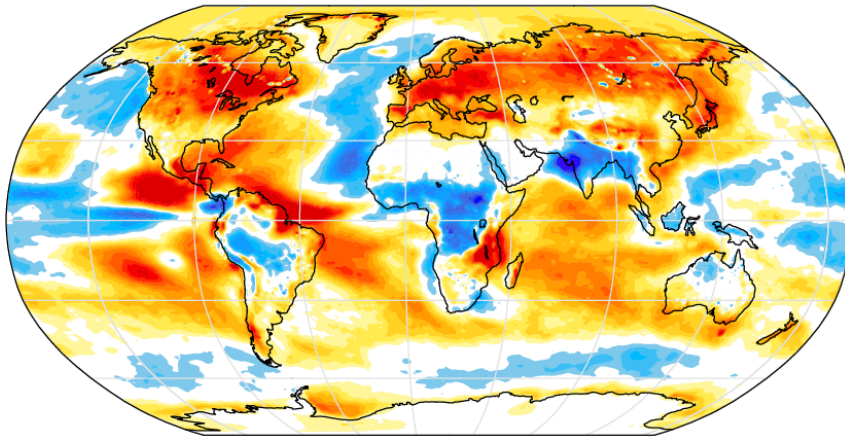
**Figure 3.** Normalized response in net top-of-atmosphere radiation (FSNT) estimated from the change between 2020-39 and 2050-69 per degree global warming for unmitigated (a) CESM1-WACCM5-RCP85 and (b) CESM2-WACCM6-SSP585 simulations, and (c) their difference (b-a). Also shown is (d) the analogous difference for the CESM1-LE and CESM2-LE and (e) the CESM2-RCP85 and CESM2-LE (scaled by 4). The difference between the geoengineered climate states in ARISE-SAI-1.5 and GLENS-SAI is shown in (f). Units for all panels are  $\text{W m}^{-2} \text{K}^{-1}$ , except in (f) where units are  $\text{W m}^{-2}$ , and stippled regions

indicate differences that exceed twice the ensemble standard error.

A) CESM1 Rapid Adj : FSNT  $\Delta^{NH-SH} = 2.4$   $W m^{-2}$



B) CESM2 Rapid Adj: FSNT  $\Delta^{NH-SH} = 0.4$   $W m^{-2}$



C) CESM2-CESM1  $\Delta^{CESM2-CESM1} = -2.0$   $W m^{-2}$

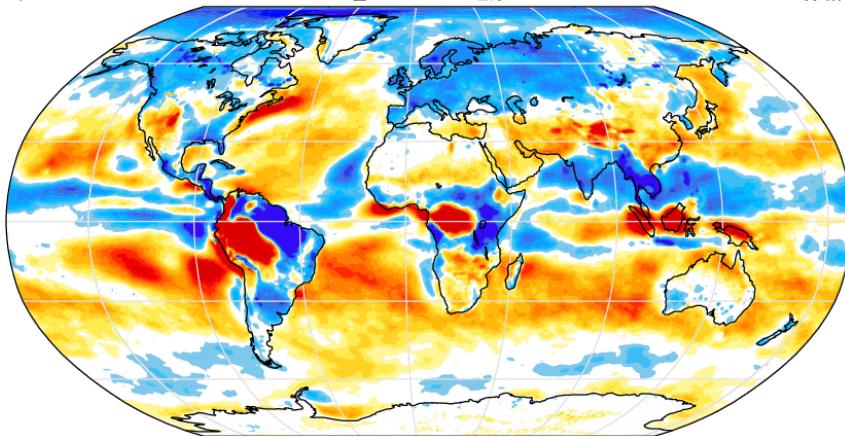
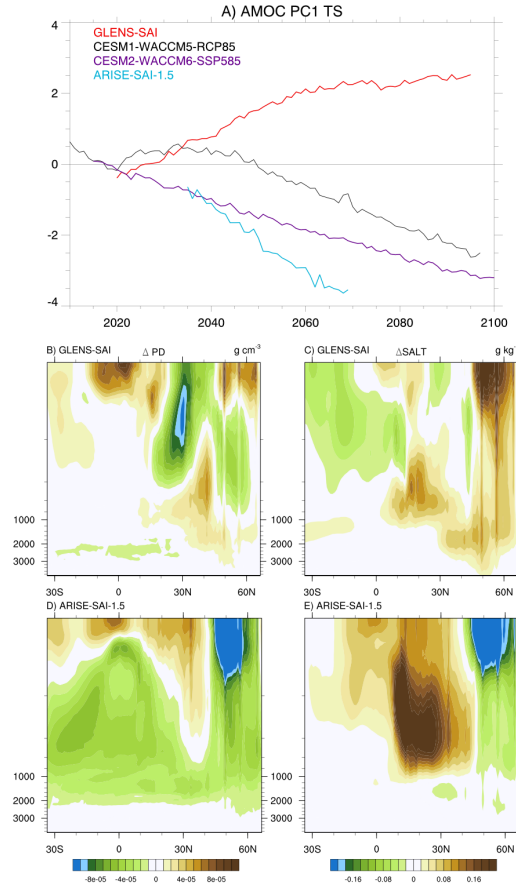


Figure 4: Estimates of the rapid adjustment of TOA net SW flux to  $\text{CO}_2$  for CESM1 (a), CESM2 (b), and their difference (c) based on estimates from 4x $\text{CO}_2$ AMIP and AMIP simulations. Differences in the hemispheric means are shown in panel titles. All units are  $\text{W m}^{-2}$ .



**Figure 5.** (a) Changes in the leading principal component of the Atlantic Meridional Overturning Circulation in unmitigated (CESM1-WACCM5-RCP85, CESM2-WACCM6-SSP585) and mitigated (GLENS-SAI, ARISE-SAI-1.5) experiments. Also shown are changes in the latitude-depth structure in the Atlantic Ocean of ocean potential density (PD, b, d, units of  $\text{g cm}^{-3}$ ) and salinity (SALT, c, e, units of  $\text{g kg}^{-1}$ ) for GLENS-SAI (b, c) and ARISE-SAI-1.5 (d, e), respectively.

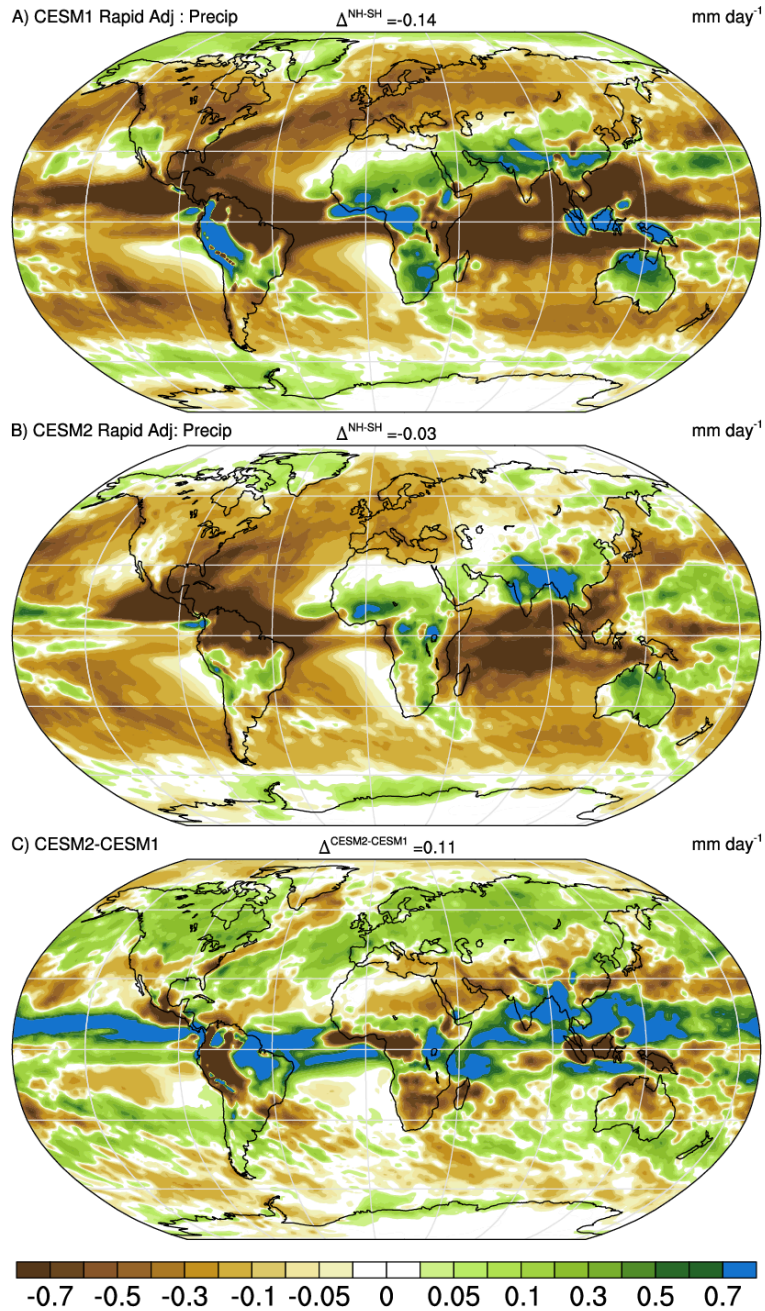


Figure 6: The rapid adjustment of total precipitation to CO<sub>2</sub> quadrupling for CESM1 (a), CESM2 (b), and their difference (c) based on estimates from 4xCO<sub>2</sub>AMIP and AMIP simulations. Differences in the hemispheric means are shown in panel titles. All units are mm day<sup>-1</sup>.

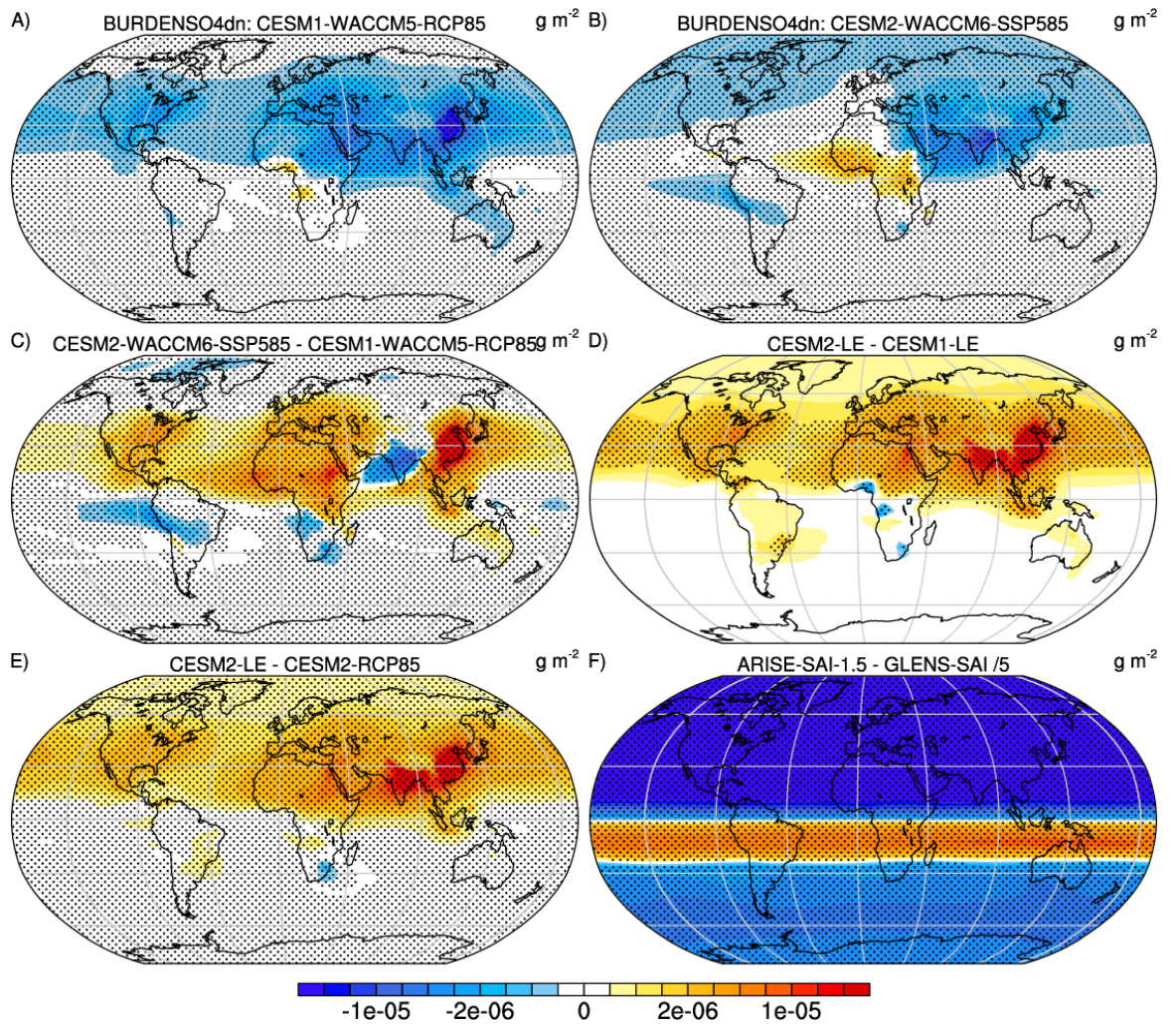


Figure 7. Absolute change in sulfate aerosol burdens (BURDENSO4dn) estimated from the difference between 2020-39 and 2050-69 for unmitigated (a) CESM1-WACCM5-RCP85 and (b) CESM2-WACCM6-SSP585 simulations, and (c) their difference (b-a). Also shown is (d) the analogous difference for the CESM1-LE and CESM2-LE and (e) the CESM2-RCP85 and CESM2-LE. The difference between the geo-engineered climate states in ARISE-SAI-1.5 and GLENS-SAI is shown in (f). Units for all panels are  $\text{g m}^{-2}$  and stippled regions indicate differences that exceed twice the ensemble standard error. The difference field in (f) is scaled by  $1/5^{\text{th}}$ .

## Figure Captions

**Figure 1.** Evolution of yearly injection mass ( $\text{Tg SO}_2 \text{ yr}^{-1}$ ) over time at the four injection latitudes for (a) GLENS-SAI and (b) ARISE-SAI-1.5 from 2035 to 2070.

**Figure 2.** Normalized response in near surface air temperature (TREFHT) estimated from the change between 2020-39 and 2050-69 per degree global warming for unmitigated (a) CESM1-WACCM5-RCP85 and (b) CESM2-WACCM6-SSP585 simulations, and (c) their difference (b-a). Also shown is (d) the analogous difference for the CESM1-LE and CESM2-LE and (e) the CESM2-RCP85 and CESM2-LE (scaled by 4). The difference between the geoengineered climate states in ARISE-SAI-1.5 and GLENS-SAI is shown in (f). Units for all panels are  $\text{K K}^{-1}$ , except in (f) where units are  $\text{W m}^{-2}$ , and stippled regions indicate differences that exceed twice the ensemble standard error.

**Figure 3.** Normalized response in net top-of-atmosphere radiation (FSNT) estimated from the change between 2020-39 and 2050-69 per degree global warming for unmitigated (a) CESM1-WACCM5-RCP85 and (b) CESM2-WACCM6-SSP585 simulations, and (c) their difference (b-a). Also shown is (d) the analogous difference for the CESM1-LE and CESM2-LE and (e) the CESM2-RCP85 and CESM2-LE (scaled by 4). The difference between the geoengineered climate states in ARISE-SAI-1.5 and GLENS-SAI is shown in (f). Units for all panels are  $\text{W m}^{-2} \text{ K}^{-1}$ , except in (f) where units are  $\text{W m}^{-2}$ , and stippled regions indicate differences that exceed twice the ensemble standard error.

**Figure 4.** Estimates of the rapid adjustment of TOA net SW flux to  $\text{CO}_2$  for CESM1 (a), CESM2 (b), and their difference (c) based on estimates from 4x $\text{CO}_2$ AMIP and AMIP simulations. Differences in the hemispheric means are shown in panel titles. All units are  $\text{W m}^{-2}$ .

**Figure 5.** (a) Changes in the leading principal component of the Atlantic Meridional Overturning Circulation in unmitigated (CESM1-WACCM5-RCP85, CESM2-WACCM6-SSP585) and mitigated (GLENS-SAI, ARISE-SAI-1.5) experiments. Also shown are changes in the latitude-depth structure in the Atlantic Ocean of ocean potential density (PD, b, d, units of  $\text{g cm}^{-3}$ ) and salinity (SALT, c, e, units of  $\text{g kg}^{-1}$ ) for GLENS-SAI (b, c) and ARISE-SAI-1.5 (d, e), respectively.

**Figure 6.** The rapid adjustment of total precipitation to  $\text{CO}_2$  quadrupling for CESM1 (a), CESM2 (b), and their difference (c) based on estimates from 4x $\text{CO}_2$ AMIP and AMIP simulations. Differences in the hemispheric means are shown in panel titles. All units are  $\text{mm day}^{-1}$ .

**Figure 7.** Absolute change in sulfate aerosol burdens (BURDEN $\text{SO}_4$ dn) estimated from the difference between 2020-39 and 2050-69 for unmitigated (a) CESM1-WACCM5-RCP85 and (b) CESM2-WACCM6-SSP585 simulations, and (c) their difference (b-a). Also shown is (d) the analogous difference for the CESM1-LE and CESM2-LE and (e) the CESM2-RCP85 and CESM2-LE.

The difference between the geoengineered climate states in ARISE-SAI-1.5 and GLENS-SAI is shown in (f). Units for all panels are  $\text{g m}^{-2}$  and stippled regions indicate differences that exceed twice the ensemble standard error. The difference field in (f) is scaled by  $1/5^{\text{th}}$ .

**Figure S1:** Normalized response in net top-of-atmosphere radiative flux (RTMT) estimated from the change between 2020-39 and 2050-69 per degree global warming for unmitigated (a) CESM1-WACCM5-RCP85 and (b) CESM2-WACCM6-SSP585 simulations, and (c) their difference (b-a). Also shown is (d) the analogous difference for the CESM1-LE and CESM2-LE and (e) the CESM2-RCP85 and CESM2-LE (scaled by 4). The difference between the geoengineered climate states in ARISE-SAI-1.5 and GLENS-SAI is shown in (f). Units for all panels are  $\text{W m}^{-2} \text{K}^{-1}$ , except in (f) where units are  $\text{W m}^{-2}$ , and stippled regions indicate differences that exceed twice the ensemble standard error.

Figure S2: Normalized response in outgoing top-of-atmosphere longwave flux (FLNT) per degree global warming estimated from the change between 2020-39 and 2050-69 for unmitigated (a) CESM1-WACCM5-RCP85 and (b) CESM2-WACCM6-SSP585 simulations, and (c) their difference (b-a). Also shown is (d) the analogous difference for the CESM1-LE and CESM2-LE and (e) the CESM2-RCP85 and CESM2-LE (scaled by 4). The difference between the geoengineered climate states in ARISE-SAI-1.5 and GLENS-SAI is shown in (f). Units for all panels are  $\text{W m}^{-2} \text{K}^{-1}$ , except in (f) where units are  $\text{W m}^{-2}$ , and stippled regions indicate differences that exceed twice the ensemble standard error.

Figure S3: Rapid adjustments of cloud amount (%) to  $\text{CO}_2$  based on 4x $\text{CO}_2$ AMIP-AMIP simulation differences in (a) CESM1, (b) CESM2, and (c) their difference (b-a).

Figure S4: Slow responses of FSNT ( $\text{W m}^{-2}$ ) to  $\text{CO}_2$  estimated from abrupt4x $\text{CO}_2$  simulations in CESM1 (a), and computed directly from AMIP+4K-AMIP simulation differences in CESM2 (b). The hemispheric contrasts are large for CESM1 ( $-2.3 \text{ W m}^{-2}$ ) and small for CESM2 ( $0.1 \text{ W m}^{-2}$ ).

Figure S5: Timeseries of hemispheric mean fluxes (a) and their differences (b) in abrupt4x $\text{CO}_2$  simulations.

Figure S6: Response in surface salinity estimated from the change between 2020-39 and 2050-69 for unmitigated (a) CESM1-WACCM5-RCP85 and (b) CESM2-WACCM6-SSP585 simulations, and their difference (c). Also shown is the analogous difference for (d) the CESM1-LE and CESM2-LE (d) and (e) the CESM2-RCP85 and CESM2-LE. The difference between the geoengineered climate states in ARISE-SAI-1.5 and GLENS-SAI is shown in (f).

Figure S7: Rapid adjustments of precipitation ( $\text{mm day}^{-1}$ ) to  $\text{CO}_2$  based on 4x $\text{CO}_2$ AMIP-AMIP simulation differences in (a) CESM1, (b) CESM2, and (c) their difference (b-a).

1 **Scenario and Model Dependence of Strategic Solar Climate Intervention in CESM**

2 **J. T. Fasullo<sup>1</sup> and J. H. Richter<sup>1</sup>**

3

4 <sup>1</sup>National Center for Atmospheric Research, Boulder, CO, 80301.

5 Corresponding author: Dr. John Fasullo ([fasullo@ucar.edu](mailto:fasullo@ucar.edu))

6

7 **Key Points:**

8 • A substantial contrast in the meridional structure of stratospheric aerosols exists in two  
9 recent climate intervention experiments.

10 • Differences in the representations of clouds and the Atlantic Meridional Overturning  
11 Circulation are identified as key drivers of the contrast.

12 • The results portend significant uncertainty in the distribution of sulfate gas injections  
13 associated with strategic climate intervention.  
14

## 15 **Abstract**

16 Model dependence in simulated responses to stratospheric aerosol injection (SAI) is a major  
17 uncertainty surrounding the potential implementation of this solar climate intervention strategy.  
18 We identify large differences in the aerosol mass latitudinal distributions between two recently  
19 produced climate model SAI large ensembles, despite using similar climate targets and controller  
20 algorithms, with the goal of understanding the drivers of such differences. Using a hierarchy of  
21 recently produced simulations, we identify three main contributors including: 1) the rapid  
22 adjustment of clouds and rainfall to elevated levels of carbon dioxide, 2) the associated low-  
23 frequency dynamical responses in the Atlantic Meridional Overturning Circulation, and 3) the  
24 contrasts in future climate forcing scenarios. Each uncertainty is unlikely to be significantly  
25 narrowed over the likely timeframe of a potential SAI deployment if a 1.5C target is to be met.  
26 The results thus suggest the need for significant flexibility in climate intervention deployment in  
27 order to account for these large uncertainties in the climate system response.

## 28 **Plain Language Summary**

29 The continued high levels of anthropogenic greenhouse gas emissions increase the likelihood  
30 that key climate warming thresholds will be exceeded in the coming decades unless some form  
31 of climate intervention is implemented. It is in this context that we examine a recently proposed  
32 approach to stratospheric aerosol injection. Using two recently produced climate model  
33 experiments, we find the associated latitudinal distribution of aerosol mass to exhibit substantial  
34 uncertainty, suggesting the need for significant flexibility in the location and amount of aerosol  
35 delivery. The uncertainty's origins stem mainly from simulated climate responses to increases in  
36 carbon dioxide including rapid adjustments in clouds and rainfall, and changes in the overturning  
37 ocean circulation. Uncertainty in future anthropogenic emissions of industrial sulfate aerosols  
38 also contribute.

## 39 **1 Introduction**

40 Solar climate intervention (SCI), or solar geoengineering, has been proposed as a means  
41 of reducing the adverse impacts of climate change via the artificial enhancement of Earth's  
42 albedo. One SCI method proposed to temporarily offset anthropogenic warming and associated  
43 impacts is stratospheric aerosol injection (SAI), which involves the delivery of aerosols or  
44 precursor gases into the stratosphere. A major uncertainty surrounding the enactment of SAI is  
45 the climate system response to both continued emissions of carbon dioxide and prolonged  
46 elevated levels of stratospheric sulfate aerosols.

47 It is in the context of this uncertainty that the National Academies of Sciences,  
48 Engineering, and Medicine (NASEM) recently called for further research to understand various  
49 SCI approaches (NASEM, 2021) as SAI has been shown, in principle, to be a method of global  
50 climate intervention capable of achieving various temperature-based targets (Tilmes et al. 2018,  
51 MacMartin et al. 2019, Simpson et al. 2019). However, there remain large uncertainties in  
52 associated climate responses and impacts (Fasullo et al. 2018, Kravitz and MacMartin 2020) and  
53 adverse effects have been identified involving the water cycle and circulations in the  
54 troposphere, stratosphere, and ocean (Tilmes et al. 2018, Kawatani et al. 2011, Watanabe and  
55 Kawatani 2012, Fasullo et al. 2018, Xu et al. 2020, Xie et al. 2021, Sun et al. 2020, Abiodun et  
56 al. 2021, Banerjee et al. 2021 Krishnamohan and Bala 2022).

57 Climate models are an essential tool for exploring the potential benefits and impacts of  
58 the broad range of proposed SAI approaches. They depict the interactions between multiple  
59 processes involved in the climate response and simulate impact-relevant fields. They also  
60 provide a process-based understanding of response mechanisms and timescales. Due to the large  
61 internal variability of the climate system, the evaluation of SAI approaches often requires climate  
62 model large ensembles (Deser et al., 2012, Kay et al. 2015, Maher et al. 2021) using Earth  
63 system models (ESMs) capable of accurately representing a diverse set of processes involving  
64 stratospheric and tropospheric dynamics and chemistry, and time-varying aerosol distributions,  
65 aspects that are well-represented in only a few currently available ESMs (Franke et al. 2021).

66 While some recent work has found broad consistency in simulated responses to simple  
67 SAI depictions, such as solar dimming (e.g. Kravitz et al. 2021, Vioni et al. 2021), this work  
68 identifies and explores substantial climate response dependencies to a more realistic SAI  
69 representation based on explicitly resolved stratospheric aerosol injections, their evolving aerosol  
70 size distributions and burdens, their interactions with dynamical, chemical, and hydrologic  
71 processes, and related couplings between the land, atmosphere, ocean, and cryosphere  
72 (MacMartin et al. 2017, Tilmes et al. 2018, Richter et al. 2022). In this work, we explore the  
73 origin of inter-model differences and their physical bases. The models, experiments, and  
74 methods used are described in Section 2. The spatial and temporal structure of injected aerosols  
75 and climate responses are presented and discussed in Section 3 while the broader consequences  
76 for the potential implementation of SAI, and suggestions for future work, are presented in  
77 Section 4.

## 78 **2 Materials and Methods**

### 79 **2.1 Models**

80 With the goal of explicitly representing the dynamical, chemical, and hydrological  
81 aspects of the climate response to SAI, this work uses versions 1 and 2 of the Community Earth  
82 System Model (CESM1, CESM2). Both versions can be run in so-called high-top and low-top  
83 atmospheric configurations. The CESM1 high-top configuration uses the Whole Atmosphere  
84 Community Climate Model, version 5 (CESM1-WACCM5, Mills et al., 2017) as its atmospheric  
85 component and the CESM2 uses WACCM6 (CESM2-WACCM6, Gettelman et al. 2019). For  
86 the atmosphere, CESM1-WACCM5 has zonal and meridional resolutions of 0.9° and 1.25°,  
87 respectively, with 70 vertical levels and a model top of 140 km. The configuration allows for a  
88 full representation of stratospheric dynamics and has extensive middle atmospheric chemistry,  
89 and is a key improvement upon earlier model generations and many current climate models (e.g.,  
90 Ferraro et al., 2015). Tropospheric physics in WACCM5 are the same as in the lower top  
91 configuration, the Community Atmosphere Model version 5 (CAM5, Park et al. 2014), the  
92 atmospheric component of the CESM1 (Hurrell et al. 2013). CESM1-WACCM5 explicitly  
93 simulates sulfate aerosol concentrations and size distributions via the Modal Aerosol Module  
94 (MAM3; Mills et al., 2017). Associated responses in ozone concentrations have a beneficial  
95 impact on the stratospheric circulation and its biennial variability (Richter et al., 2017) and these  
96 have been shown to reduce the CO<sub>2</sub>-driven midlatitude jets' poleward shift under present-day  
97 climate change (Chiodo and Polvani, 2019). Confidence in the representations of sulfate aerosol  
98 processes and their radiative effects are bolstered by the relatively close agreement that exists  
99 between simulated and observed radiative responses to the 1991 eruption of Mount Pinatubo  
100 (Mills et al., 2017). The ocean component of all models used in this study is the Parallel Ocean

101 Program version 2 (POP2; Smith et al., 2010; Danabasoglu et al., 2012), which as uniform zonal  
102 resolution of  $1.125^\circ$ , and variable meridional resolution ranging from  $0.27^\circ$  in the tropics to  $0.64^\circ$   
103 in the extratropical northern hemisphere. The model has 60 vertical levels with a uniform  
104 resolution of 10 m in the ocean's upper 160 m.

105 CESM2-WACCM6 incorporates various advances including fully interactive  
106 tropospheric chemistry and an interactive crop model. Tropospheric physics is largely the same  
107 as in the low-top configuration, the Community Atmosphere Model version 6 (CAM6) as a  
108 concerted effort was made during development of these models to use the same model tuning in  
109 the low-top and high-top configurations in order to promote inter-version comparison (Gettelman  
110 et al. 2019). CAM6 is the atmospheric component of CESM2 (Danabasoglu et al. 2020) and  
111 uses the Cloud Layers Unified By Binormals (CLUBB; Golaz et al., 2002; Larson, 2017) unified  
112 turbulence scheme and the updated Morrison-Gettelman microphysics scheme (MG2; Gettelman  
113 and Morrison, 2015). Minor changes to POP2 are incorporated in CESM2-WACCM6  
114 (Danabasoglu et al., 2020).

## 115 2.2 CESM1-WACCM5 Simulations

116 A summary of design characteristics for the simulations used here are given in Table 1.  
117 We use CESM1-WACCM5 SAI simulations that are a part of the Geoengineering Large  
118 Ensemble (GLENS, Tilmes et al., 2018). GLENS consists of two large ensemble of simulations:  
119 one without and one with SAI. Both ensembles use the Representative Concentration Pathway  
120 8.5 (RCP85) emissions scenario for greenhouse gases. The baseline GLENS simulations consists  
121 of free running RCP85 simulations from 2005 through 2030 (17 members), with an additional 3  
122 members continuing through 2100 (CESM1-WACCM5-RCP85). The second set of GLENS  
123 simulations, GLENS-SAI, utilizes strategically enacted SAI (following Kravitz et al. 2017),  
124 which consists of twenty members from 2020 to 2097 in which aerosol injections are specified  
125 by a controller algorithm (MacMartin et al. 2014, Kravitz et al. 2017) to achieve stabilization of  
126 temperature targets at their mean 2020 conditions under RCP85. The targets include near-surface  
127 air temperature's global mean, equator-to-pole gradient, and inter-hemispheric gradient, which  
128 are all successfully stabilized in GLENS-SAI, though the equator-to-pole gradient increases  
129 slightly (by about 0.1 K from 2050 to 2070, Tilmes et al. 2018). The predefined injection  
130 latitudes for GLENS-SAI are  $15^\circ$  and  $30^\circ$  in each hemisphere and  $\text{SO}_2$  is injected about 5 km  
131 above the tropopause, or approximately 25 and 23 km for the  $15^\circ$  and  $30^\circ$  sites, respectively, with  
132 an arbitrarily chosen longitude of  $180^\circ$  (Tilmes et al. 2018). The initialization of GLENS-SAI is  
133 made from three distinct members of the RCP85 experiment, which itself branched from distinct  
134 historical-era simulations, thus providing a diversity of initialized ocean states. GLENS has been  
135 used in a range of contexts (Fasullo et al. 2018, Simpson et al. 2019, Pinto et al., 2020, Da-  
136 Allada et al, 2020).

## 137 2.3 CESM2-WACCM6 Simulations

138 As with GLENS, we use two sets of CESM2-WACCM6 experiments. The CESM2-  
139 WACCM6 baseline simulations used are from the Coupled Model Intercomparison Project  
140 version 6 (CMIP6, Eyring et al. 2016) and the Assessing Responses and Impacts of Solar climate  
141 intervention on the Earth system with Stratospheric Aerosol Injection project ARISE-SAI,  
142 Richter et al. 2022). These include the unmitigated CMIP6 SSP585 simulations, to allow for  
143 comparison with the RCP85 experiments in GLENS (Tilmes et al. 2020). The second experiment

144 used is the SAI ensemble, with strategically placed sulfur dioxide injection to keep the global  
145 mean temperature at  $\sim 1.5$  C over preindustrial temperatures (ARISE-SAI-1.5, Richter et al.  
146 2022). These simulations extend from 2035 to 2069 and use the same controller algorithm and  
147 target metrics as GLENS-SAI, but for the 2020-2039 time average in the unmitigated CESM2-  
148 WACCM6 baseline simulations, in contrast to GLENS-SAI where targets are based on the 2010  
149 – 2030 time period. Target metrics are successfully met in ARISE-SAI-1.5 to within 0.05 K over  
150 the period 2050 to 2070 (Richter et al. 2022). The injections are again at  $15^\circ$  and  $30^\circ$  in both  
151 hemispheres and at an arbitrarily chosen longitude of  $180^\circ$ , as in GLENS-SAI, but occur lower in  
152 the stratosphere (approximately 21 km). The slight difference in injection height between  
153 GLENS-SAI and ARISE-SAI doesn't significantly impact their efficacy however as the  
154 shortwave optical depth of the stratosphere is small relative to the troposphere. Moreover, single  
155 point injections result in strong similarity in the latitudinal structure of aerosol optical depth  
156 between CESM1 (Tilmes et al., 2017) and CESM2 (Visioni et al., 2022), with circulation  
157 differences and lifetime effects contributing to slightly greater aerosol optical depths in GLENS  
158 (Visioni et al. 2022). ARISE-SAI-1.5 simulations use the moderate Shared Socioeconomic  
159 Pathway (SSP) scenario of SSP245 for its defacto future scenario (Burgess et al., 2020), a  
160 moderate scenario where “the world follows a path in which social, economic, and technological  
161 trends do not shift markedly from historical patterns” (O'Neill et al. 2016). The temperature  
162 targets for ARISE-SAI-1.5 are based on the same regional metrics as used in GLENS-SAI and  
163 the simulations consist of a 10-member ensemble.

#### 164 2.4 Additional Simulations

165 In order to gain insight into the drivers of contrasts between the above SAI simulations,  
166 we use additional experiments. Below the stratosphere, CAM5 and CAM6 use physical  
167 representations of the climate system that are highly similar to their WACCM counterparts.  
168 Simulations using them therefore provide a means for inferring the tropospheric contribution to  
169 contrasts in our SAI experiments. For example, the ensemble mean of the CESM1 and CESM2  
170 large ensembles (LE) provides an estimate of the future forced response (to both warming and  
171  $\text{CO}_2$  increases) by averaging across members, and through internally driven variability.  
172 Simulations used here include the 40-member CESM1-LE (Kay et al. 2015) and 100-member  
173 CESM2-LE (Rodgers et al. 2021), and a 10-member ensemble of CESM2 that makes use of  
174 CMIP5 historical and RCP85 prescribed forcing agents, (CESM2-RCP85, Forster et al. 2013).  
175 These large ensembles extend from 1850 to 2100, though for the CESM1-LE and CESM2-  
176 RCP85 only a single member spans 1850-1920. Also notable is the fact that the CESM2-LE uses  
177 SSP370 for its future scenario, rather than the SSP245 used in ARISE or the SSP585 used in  
178 future CESM2-WACCM6 simulations, and these differences complicate direct comparisons, as  
179 discussed further below. SSP370 represents the medium to high end of plausible future pathways  
180 and represents a forcing level common to several unmitigated SSP baselines

181 To quantify rapid adjustments to  $\text{CO}_2$ , those that occur in the absence of surface warming  
182 (e.g. Tilmes et al. 2013), idealized experiments using CESM1 and CESM2 are also used in  
183 which  $\text{CO}_2$  is quadrupled in both fixed sea surface temperature (SST, 4x $\text{CO}_2$ AMIP) and coupled  
184 ocean (Abrupt4x $\text{CO}_2$ ) frameworks. Conversely, slow responses to warming are those that ensue in  
185 response to surface warming when  $\text{CO}_2$  levels and other climate forcing agents are fixed, and  
186 these are estimated from so-called AMIP+4K experiments where uniform SST increases of 4 K  
187 are imposed on an AMIP background state. For these sensitivity experiments, the accompanying  
188 AMIP and pre-industrial coupled experiments are used to estimate ‘control’ conditions.

189 Together, these simulations allow for the estimation of both so-called “rapid adjustments” to CO<sub>2</sub>  
190 and “slow responses” to warming, and these are found to provide important insight into contrasts  
191 between GLENS and ARISE. Rapid adjustments also exist for other climate forcings, such as  
192 aerosols, and in the stratosphere these effects can be significant locally (Richter et al. 2017). On  
193 planetary scales however these have been shown generally to be small relative to the adjustment  
194 to CO<sub>2</sub> (Andrews et al., 2009; Bala et al., 2010; Samset et al., 2016; Tilmes et al., 2013).

### 195 **3 Results**

196 The yearly stratospheric aerosol mass injections specified in GLENS-SAI and ARISE-  
197 SAI-1.5 are shown in Figure 1, where we examine the common period of 2035 to 2069 (Table  
198 1). The greater total emissions in GLENS-SAI than ARISE-SAI-1.5 are expected as they  
199 correspond to greater total offset CO<sub>2</sub> concentrations. However less expected is the large  
200 disparity in the latitudinal distribution of injections, with the vast majority of GLENS-SAI  
201 aerosols injected at 30°N and 30°S, with modest injection amounts occurring at 15°N and  
202 negligible injection mass at 15°S. This contrasts starkly with ARISE-SAI-1.5, where injections  
203 occur overwhelmingly at 15°S, with much smaller injection amounts at 15°N and 30°S, and  
204 negligible injection mass at 30°N. These relative proportions and their contrasts are  
205 approximately constant over time from 2035 to 2069, suggesting that they are relatively  
206 insensitive to the associated total avoided warming or the control period used for climate targets.  
207 Rather the persistence of the distributions over time suggests the possibility of an intrinsic  
208 contrast in the climate responses between the two ensembles.

209 To explore the processes that may underlie the contrasts in Fig. 1, the normalized  
210 structure of warming in a range of additional simulations is examined in Figure 2. Normalized  
211 warming patterns from 2020-39 and 2050-69 in the associated unmitigated simulations (i.e.  
212 CESM1-WACCM5-RCP85 and CESM2-WACCM6-SSP585) show various features expected  
213 under anthropogenic climate change such as greater warming over land and in polar regions (Fig.  
214 2a, b). Differences between the experiments are also clearly evident, particularly in the northern  
215 hemisphere (NH) extratropics, where warming is stronger in CESM1-WACCM5-RCP85 and a  
216 strong cooling in the North Atlantic (NATL) is evident in CESM2-WACCM6-SSP585.  
217 Differencing the normalized warming patterns (Fig. 2c) highlights systematically weaker  
218 warming in the NH in CESM2-WACCM6-SSP585 and stronger warming in the southern  
219 hemisphere (SH) subtropics, particularly in the subtropical stratocumulus cloud deck regions in  
220 the eastern ocean basins. When the analogous difference is computed between the CESM1-LE  
221 and CESM2-LE (Fig. 2d) a similar overall pattern emerges, albeit with slightly weaker  
222 magnitudes in the extratropical NH and SH. The strong similarities of patterns in Fig. 2c/d  
223 suggest a potentially dominant contribution from tropospheric physics in CAM5 and CAM6,  
224 which as discussed earlier are shared by their WACCM counterparts. The existence of  
225 differences between Figs. 2c/d suggests a potential role for both WACCM physics and scenario  
226 contrasts between the ensembles. The role of scenario can be estimated by examining differences  
227 between CESM2-RCP85 and CESM2-LE (Fig. 2e, note the scaling used). The persisting  
228 negative differences in the NH and positive differences in the SH subtropics suggest that the  
229 contrasts between SSP370, which is the future scenario used for the CESM2-LE (Fig. 2d), and  
230 RCP85 contribute to the pattern in Fig. 2d but are not the dominant contributor to it. Given this,  
231 potential contributors to the pattern are explored further below. Also notable is the result that  
232 various features of the unmitigated warming contrast between CESM1-WACCM5-RCP85 and  
233 CESM2-WACCM6-SSP585 (Fig. 2c) are shared by the differences in SAI regional warming

234 patterns (Fig. 2f), such as the elevated warming in the southern subtropics, and relative cooling  
235 in the NATL and NH subpolar regions, in ARISE-SAI-1.5 relative to GLENS-SAI, suggesting  
236 that these features may be intrinsic model responses.

237 To further explore the origin of model responses, changes in top-of-atmosphere (TOA)  
238 absorbed solar radiation (FSNT) are assessed and found to be strongly tied to patterns of  
239 warming. In unmitigated CESM1-WACCM5-RCP85 and CESM2-WACCM6-SSP585  
240 simulations (Fig. 3a, b) normalized increases in FSNT are widespread, consistent with 21<sup>st</sup>  
241 century climate projections generally (Trenberth and Fasullo, 2009). However the inter-model  
242 difference (Fig. 3c) shows a strong spatial correlation with contrasting patterns of warming (Fig.  
243 2c) as stronger SH subtropical warming in CESM1-WACCM5-RCP85 is accompanied by  
244 disproportionate FSNT increases while enhanced NATL cooling is coincident with FSNT  
245 decreases. When normalized patterns in the CESM1-LE and CESM2-LE are compared (Fig. 3d),  
246 a similar general pattern of FSNT differences exists, albeit slightly weaker, again suggesting the  
247 patterns to be an intrinsic feature of CAM5 and CAM6, with a potential secondary contribution  
248 from WACCM or scenario contrasts. When the CESM2-LE is compared to CESM2-RCP85 a  
249 similar but significantly weaker pattern of differences is evident (Fig. 3e, note the scaling used),  
250 suggesting a modest but detectible role for the future scenario in driving contrasts between the  
251 simulations. Unlike the temperature response under SAI, the difference pattern of FSNT change  
252 between ARISE-SAI-1.5 and GLENS-SAI is not strongly correlated with that of the unmitigated  
253 simulations and instead largely reflects the combined and complex influence of changes in  
254 clouds and SAI (Fig. 3f).

255 Various additional analyses provide important background for interpreting contrasts in  
256 our SAI experiments. In Fig. 3, a focus on changes in patterns of FSNT is motivated by their  
257 dominant contribution to the overall pattern of net TOA flux (Fig. S1). While changes in  
258 outgoing longwave radiation exist (Fig. S2), these can generally be viewed as responding to  
259 differences in warming, rather than driving them, as they are positively correlated to temperature  
260 anomalies and thus offset, in many cases, changes in FSNT. Understanding the origin of spatial  
261 patterns and interhemispheric FSNT gradients in unmitigated simulations is therefore critical to  
262 anticipating the latitudinal distribution of injection amounts under SAI.

263 In this context the 4xCO<sub>2</sub>AMIP and Abrupt4xCO<sub>2</sub> simulations provide important insight  
264 as they demonstrate that responses in shortwave radiation and clouds to elevated levels of CO<sub>2</sub>  
265 (i.e. rapid adjustments) also differ considerably between CESM1 and CESM2 in a way that is  
266 consistent with the need for greater NH mitigation in the GLENS-SAI experiment. For example,  
267 in CESM1 there is a strong hemispheric gradient in FSNT rapid adjustments (Fig. 4) such that  
268 the NH absorbs 2.4 W m<sup>-2</sup> more energy than the SH in response to a CO<sub>2</sub> quadrupling. In  
269 contrast, in CESM2 the response is relatively symmetric between hemispheres with an imbalance  
270 of only 0.4 W m<sup>-2</sup>, with strong warming contributions evident in the SH subtropics, as also  
271 identified as being key in Figs. 2, 3. These experiments therefore show that rapid adjustments are  
272 likely an important contributor to the patterns in unmitigated simulations and to injection mass  
273 contrasts between GLENS-SAI and ARISE-SAI-1.5, as CO<sub>2</sub> levels continue to increase in these  
274 simulations. Moreover, the radiation contrasts can be linked to rapid adjustments in clouds, with  
275 reductions in cloud amount in the southern hemisphere subtropics being closely tied to  
276 associated increases in FSNT. It is also notable that the hemispheric contrasts in the slow  
277 responses to warming also contrast significantly between models, with the pattern in CESM1  
278 being hemispherically asymmetric and offsetting rapid adjustments, and the pattern in CESM2

279 being approximately symmetric (Fig. S4). While regional features are more difficult to interpret  
280 in fully coupled simulations due to the presence of coupled internal variability, it is noteworthy  
281 that disproportionate FSNT increases in the NH also emerge in the early years of Abrupt4xCO<sub>2</sub>  
282 experiments and these are sustained for several decades. Together these findings highlight the  
283 need to understand the sensitivity of the climate response directly to CO<sub>2</sub> if uncertainties in the  
284 implementation of SAI are to be reduced.

285 Contrasting warming patterns in the Atlantic Ocean are also suggestive of the  
286 involvement of an additional important component of the energy budget, the Atlantic Meridional  
287 Overturning Circulation (AMOC), which transports heat northward in the Atlantic and  
288 redistributes ocean mass, nutrients, salinity, and energy globally (Zhang et al. 2019). Differences  
289 between the response in AMOC in our experiments are explored in Figure 5. Changes in the  
290 strength of the leading mode of AMOC (Fig. 5a) contrast considerably across the experiments. In  
291 GLENS-SAI, the intensity of AMOC increases and this drives an associated enhanced northward  
292 transport of heat into the NATL (Fasullo et al. 2018). The strengthening contrasts however with  
293 all other simulations considered here (Fig. 5a) and with unmitigated climate projections  
294 generally (Zhang et al. 2019, Xie et al. 2021), where AMOC typically weakens during the 21<sup>st</sup>  
295 century. A similar decrease in intensity is evident between ARISE-SAI-1.5 and the unmitigated  
296 CESM1-WACCM5-RCP85 and CESM2-WACCM-SSP585. A key driver of AMOC's leading  
297 mode is deep water formation in the NATL and in this region simulation of ocean density and  
298 salinity also differ substantially between the various experiments. In GLENS-SAI, the subpolar  
299 NATL becomes denser and more saline (Fig 5b, 5c) while the subtropical north Atlantic Ocean  
300 becomes less dense. These changes accompany increases in evaporation and a net negative  
301 surface freshwater flux, which enhances salinity and density (Fasullo et al. 2018). In ARISE-  
302 SAI-1.5 the situation is reversed, with the subpolar NATL becoming substantially less dense and  
303 fresher, with associated reductions in evaporation (not shown). In ARISE-SAI-1.5, density  
304 reductions are evident in the Atlantic at all latitudes below 200 to 500 m due to warming (not  
305 shown) and salinity increases are evident south of 40N, patterns that contrast markedly with  
306 GLENS-SAI. Causal connections between salinity, density, and AMOC intensity can be complex  
307 however and will be discussed further below.

308 The sensitivity of AMOC to CO<sub>2</sub> and SAI also exists as a key uncertainty. Diagnosing  
309 individual drivers of AMOC in fully coupled simulations is extremely challenging given the  
310 diversity of thermal, saline, and dynamical processes that drive its changes (Zhang et al. 2019)  
311 and achieving a full understanding of contrasts between GLENS-SAI and ARISE-SAI-1.5 is left  
312 for future work. However, various changes are simulated that are consistent with having an  
313 influence and these include the modulation of salinity and density in the NATL (Zhang et al.  
314 2022), as in ARISE-SAI-1.5 a widespread freshening and decrease in density are simulated, in  
315 contrast to salinity and density increases simulated in GLENS-SAI (Fig. S6). A similar salinity  
316 contrast is also simulated in future unmitigated simulations using CESM2-WACCM-SSP585 and  
317 CESM1-WACCM5-RCP85, and in the CESM2-LE and CESM1-LE, suggesting that the contrast  
318 is intrinsic, at least in part, to CAM5 and CAM6 structural contrasts (Fig. S6). This possibility is  
319 supported further by rapid adjustments in precipitation to CO<sub>2</sub>, as CESM2 simulates  
320 systematically weaker reductions in precipitation in the northern extratropics than does CESM1  
321 (Fig. 6), both over the Atlantic Ocean and over much of northern extratropical land where river  
322 discharge influences ocean salinity. While neither model simulates changes in rainfall that on  
323 their own would weaken AMOC, the potential for negative surface freshwater contributions to  
324 offset the elevated buoyancy driven by warming is suggested to differ considerably. More

325 precise attribution of AMOC changes and their contrasts between experiments likely requires  
326 additional targeted experiments, the results here point to a potentially important role for rapid  
327 adjustments in the water cycle.

328 Lastly, a role for the future climate scenario in influencing the latitudinal distribution of  
329 SAI injection mass is suggested by the differences between CESM2-LE and CESM2-RCP85  
330 warming and radiation patterns, given the stronger NH warming and FSNT increases east of  
331 important sulfate emissions regions in Asia in simulations using RCP85 (negative differences in  
332 Figs. 2e, 3e, S1e, S2e). This hypothesis can be explored by examining changes in atmospheric  
333 sulfate burdens (Fig. 7), which differ significantly through the 2030-70 period between the  
334 experiments used. As discussed previously, comparison across these experiments is complicated  
335 by the differences in the scenarios used in each. However, the fact that differences in the sulfate  
336 distributions across experiments are both significant and correspond directly to simulated  
337 features in radiation and temperature suggests a role as a mediating effect on SAI experiments. In  
338 general, simulations that use RCP85 emissions show stronger reductions in burdens than those  
339 that use SSP370 (Fig. 7d, e) or SSP585 (Fig. 7c). Given the strong cooling associated with the  
340 burdens via their impact on clouds, these differences constitute an anomalous NH warming  
341 contribution in the 21<sup>st</sup> C for RCP85-based experiments (Fig. 7c-e) that thus require additional  
342 NH mitigation (Fig. 7f).

#### 343 **4 Discussion and Conclusions**

344 The analysis of our climate intervention and complementary experiments highlights a  
345 fundamental and perhaps underappreciated contributor to uncertainties surrounding SAI, the  
346 rapid adjustments of the climate system to CO<sub>2</sub>. Such adjustments include both the responses of  
347 patterns in cloud fields, which drive radiation contrasts between hemispheres, and precipitation,  
348 which can influence upper ocean salinity, density, and associated ocean circulations and energy  
349 flows. As shown here, the simulation of rapid adjustments can vary considerably across models  
350 and resolving these inter-model discrepancies is thus critical in order to better constrain the  
351 design parameters of SAI if implemented in nature. Uncertainties in future scenarios must also  
352 be reduced in order to winnow the spread across SAI simulations, and progress along this front  
353 has been made in recent years with the identification of biases in prescribed CMIP6 emissions  
354 (e.g. Paulot et al. 2018, Wang et al. 2021). Notably however, the climate response uncertainty  
355 associated with prescribed sulfate emissions is magnified by the broad range with which aerosol  
356 indirect effects on clouds as represented across climate models. The inference from the SAI  
357 simulations explored here is that the latitude of SAI injections will depend explicitly on ambient  
358 anthropogenic emissions of sulfate aerosols and formulation of an SAI strategy should therefore  
359 be accompanied by well-defined industrial emissions targets.

360 There are also important limits on the results shown here. First, they are based on only  
361 two climate models, and in many respects these models share physics that is central to the  
362 representation of SAI. A broader consideration of structural model uncertainty is therefore  
363 warranted and it is likely that key sources of uncertainty, such as cloud-aerosol interactions, are  
364 not well-estimated in contrasts between our experiments. A need therefore exists for a broader  
365 multi-model effort to realistically depict SAI and its uncertainties and to coordinate associated  
366 model development efforts. Notably a vast majority of climate models currently cannot represent  
367 the diversity of associated processes and fields simulated in WACCM. Observational efforts to  
368 monitor relevant fields and guide model development activities are also crucial if the inherent

369 risks and uncertainties of SAI are to be understood, quantified, and reduced to a point where SCI  
370 might become a promising risk-mitigation measure.

371 **Acknowledgments**

372 This material is based upon work supported by the National Center for Atmospheric  
373 Research (NCAR), which is a major facility sponsored by the National Science Foundation  
374 (NSF) under Cooperative Agreement 1852977 and by SilverLining through its Safe Climate  
375 Research Initiative. The CESM project is supported primarily by the NSF. Computing and data  
376 storage resources, including the Cheyenne supercomputer (doi:10.5065/D6RX99HX), were  
377 provided by the Computational and Information Systems Laboratory (CISL) at NCAR. We thank  
378 all the scientists, software engineers, and administrators who contributed to the development of  
379 CESM2. JF was also supported by NASA Awards 80NSSC17K0565 and 80NSSC22K0046.

380 **Availability Statement**

381 All GLENS-SAI and CESM1-WACCM5-RCP85 simulations are available to the  
382 community via the Earth System Grid (see information at [www.cesm.ucar](http://www.cesm.ucar.edu/projects/community-projects/GLENS/)  
383 [.edu/projects/community-projects/GLENS/](http://www.cesm.ucar.edu/projects/community-projects/GLENS/)). Output from the CESM1-LE, CESM2-LE, CESM2-  
384 RCP85, CESM2-WACCM6-SSP585, simulations and ARISE-SAI-1.5 simulations is freely  
385 available the NCAR Climate Data Gateway at <https://doi.org/10.26024/0cs0-ev98> and  
386 <https://doi.org/10.5065/9kcn-9y79> respectively. CMIP6 data including CESM2-WACCM6-  
387 SSP585, 4xCO2AMIP, and 4xAbruptCO<sub>2</sub> simulations are available online ([https://esgf-](https://esgf-node.llnl.gov/projects/cmip6/)  
388 [node.llnl.gov/projects/cmip6/](https://esgf-node.llnl.gov/projects/cmip6/)).

389 **Author Contributions**

390 Conceptualization: J. T. Fasullo, J. H. Richter

391 Data curation: J. T. Fasullo, J. H. Richter

392 Formal analysis: J. T. Fasullo

393 Funding acquisition: J. H. Richter

394 Methodology: J. T. Fasullo, J. H. Richter

395

396

397 **References**

- 398 Abiodun, B. J., Odoulami, R. C., Sawadogo, W., Oloniyo, O. A., Abatan, A. A., New, M., ... &  
399 MacMartin, D. G. (2021), Potential impacts of stratospheric aerosol injection on drought risk  
400 managements over major river basins in Africa. *Climatic Change*, 169(3), 1-19,  
401 <https://doi.org/10.1007/s10584-021-03268-w>.
- 402 Andrews, T., Forster, P. M., & Gregory, J. M. (2009). A surface energy perspective on climate  
403 change. *Journal of Climate*, 22(10), 2557–2570. <https://doi.org/10.1175/2008JCLI2759.1>
- 404 Bala, G., Caldeira, K., & Nemani, R. (2010). Fast versus slow response in climate change:  
405 Implications for the global hydrological cycle. *Climate Dynamics*, 35(2-3), 423–434.  
406 <https://doi.org/10.1007/s00382-009-0583-y>.
- 407 Banerjee, A., Butler, A. H., Polvani, L. M., Robock, A., Simpson, I. R., & Sun, L. (2021),  
408 Robust winter warming over Eurasia under stratospheric sulfate geoengineering—the role of  
409 stratospheric dynamics. *Atmospheric Chemistry and Physics*, 21(9), 6985-6997,  
410 <https://doi.org/10.5194/acp-21-6985-2021>.
- 411 Burgess, M. G., J. Ritchie, J. Shapland & Pielke R. Jr. (2021), IPCC baseline scenarios have  
412 over-projected CO2 emissions and economic growth. *Env. Res. Lett.*, 16, 014016,  
413 <https://doi.org/10.1088/1748-9326/abcdd2>.
- 414 Chiodo, G., & Polvani, L. M. (2019), The Response of the Ozone Layer to Quadrupled CO 2  
415 Concentrations: Implications for Climate. *Journal of climate*, 32(22), 7629-7642,  
416 <https://doi.org/10.1175/JCLI-D-19-0086.1>.

- 417 Da-Allada, C. Y., Baloïtcha, E., Alamous, E. A., Awo, F. M., Bonou, F., Pomalegni, Y., ... &  
418 Irvine, P. J. (2020), Changes in west African summer monsoon precipitation under stratospheric  
419 aerosol geoengineering. *Earth's Future*, 8(7), <https://doi.org/10.1029/2020EF001595>.
- 420 Danabasoglu, G., Bates, S. C., Briegleb, B. P., Jayne, S. R., Jochum, M., Large, W. G., ... &  
421 Yeager, S. G. (2012). The CCSM4 ocean component. *Journal of Climate*, 25(5), 1361-1389,  
422 <https://doi.org/10.1175/JCLI-D-11-00091.1>.
- 423 Danabasoglu, G., Lamarque, J. F., Bacmeister, J., Bailey, D. A., DuVivier, A. K., Edwards, J., ...  
424 & Strand, W. G. (2020), The community earth system model version 2 (CESM2). *Journal of*  
425 *Advances in Modeling Earth Systems*, 12(2), <https://doi.org/10.1029/2019MS001916>.
- 426 Deser, C., Phillips, A., Bourdette, V., & Teng, H. (2012), Uncertainty in climate change  
427 projections: the role of internal variability. *Climate dynamics*, 38(3), 527-546,  
428 <https://doi.org/10.1007/s00382-010-0977-x>.
- 429 Eyring, V., Bony, S., Meehl, G. A., Senior, C. A., Stevens, B., Stouffer, R. J., & Taylor, K. E.  
430 (2016). Overview of the Coupled Model Intercomparison Project Phase 6 (CMIP6) experimental  
431 design and organization. *Geoscientific Model Development*, 9(5), 1937-1958,  
432 <https://doi.org/10.5194/gmd-9-1937-2016>.
- 433 Fasullo, J. T., Tilmes, S., Richter, J. H., Kravitz, B., MacMartin, D. G., Mills, M. J., & Simpson,  
434 I. R. (2018), Persistent polar ocean warming in a strategically geoengineered climate. *Nature*  
435 *Geoscience*, 11(12), 910-914.
- 436 Ferraro, A. J., & Griffiths, H. G. (2016), Quantifying the temperature-independent effect of  
437 stratospheric aerosol geoengineering on global-mean precipitation in a multi-model ensemble.  
438 *Environmental Research Letters*, 11(3), <https://doi.org/10.1088/1748-9326/11/3/034012>.

- 439 Forster, P. M., Andrews, T., Good, P., Gregory, J. M., Jackson, L. S., & Zelinka, M. (2013),  
440 Evaluating adjusted forcing and model spread for historical and future scenarios in the CMIP5  
441 generation of climate models. *Journal of Geophysical Research: Atmospheres*, *118*(3), 1139-  
442 1150, <https://doi.org/10.1002/jgrd.50174>
- 443 Franke, H., Niemeier, U., & Visionsi, D. (2021), Differences in the quasi-biennial oscillation  
444 response to stratospheric aerosol modification depending on injection strategy and species.  
445 *Atmospheric Chemistry and Physics*, *21*(11), 8615-8635, [https://doi.org/10.5194/acp-21-8615-](https://doi.org/10.5194/acp-21-8615-2021)  
446 2021.
- 447 Gettelman, A., Mills, M. J., Kinnison, D. E., Garcia, R. R., Smith, A. K., Marsh, D. R., ... &  
448 Randel, W. J. (2019). The whole atmosphere community climate model version 6  
449 (WACCM6). *Journal of Geophysical Research: Atmospheres*, *124*(23), 12380-12403,  
450 [10.1029/2019JD030943](https://doi.org/10.1029/2019JD030943).
- 451 Golaz, J.-C., Larson, V. E., & Cotton, W. R. (2002). A PDF-based model for boundary layer  
452 clouds. Part I: Method and model description. *Journal of the Atmospheric Sciences*, *59*, 3540–  
453 3551, [https://doi.org/10.1175/1520-0469\(2002\)059<3540:APBMFB>2.0.CO;2](https://doi.org/10.1175/1520-0469(2002)059<3540:APBMFB>2.0.CO;2).
- 454 Hurrell, J. W., Holland, M. M., Gent, P. R., Ghan, S., Kay, J. E., Kushner, P. J., ... & Marshall, S.  
455 (2013), The community earth system model: a framework for collaborative research. *Bulletin of*  
456 *the American Meteorological Society*, *94*(9), 1339-1360, [https://doi.org/10.1175/BAMS-D-12-](https://doi.org/10.1175/BAMS-D-12-00121.1)  
457 00121.1.
- 458 Kawatani, Y., Hamilton, K., & Watanabe, S. (2011). The quasi-biennial oscillation in a double  
459 CO<sub>2</sub> climate. *Journal of the Atmospheric Sciences*, *68*(2), 265-283,  
460 <https://doi.org/10.1175/2010JAS3623.1>.

- 461 Kay, J. E., Deser, C., Phillips, A., Mai, A., Hannay, C., Strand, G., ... & Vertenstein, M. (2015).  
462 The Community Earth System Model (CESM) large ensemble project: A community resource  
463 for studying climate change in the presence of internal climate variability. *Bulletin of the*  
464 *American Meteorological Society*, 96(8), 1333-1349, <https://doi.org/>.
- 465 Jackson, L. C., Biastoch, A., Buckley, M. W., Desbruyères, D. G., Frajka-Williams, E., Moat, B.,  
466 & Robson, J. (2022), The evolution of the North Atlantic Meridional Overturning Circulation  
467 since 1980. *Nature Reviews Earth & Environment*, 1-14, [https://doi.org/10.1038/s43017-022-](https://doi.org/10.1038/s43017-022-00263-2)  
468 00263-2.
- 469 Jones, A., Haywood, J. M., Jones, A. C., Tilmes, S., Kravitz, B., & Robock, A. (2021), North  
470 Atlantic Oscillation response in GeoMIP experiments G6solar and G6sulfur: why detailed  
471 modelling is needed for understanding regional implications of solar radiation management.  
472 *Atmospheric Chemistry and Physics*, 21(2), 1287-1304, [https://doi.org/10.5194/acp-21-1287-](https://doi.org/10.5194/acp-21-1287-2021)  
473 2021.
- 474 Kravitz, B., MacMartin, D. G., Vioni, D., Boucher, O., Cole, J. N., Haywood, J., ... & Tilmes,  
475 S. (2021), Comparing different generations of idealized solar geoengineering simulations in the  
476 Geoengineering Model Intercomparison Project (GeoMIP). *Atmospheric Chemistry and Physics*,  
477 21(6), 4231-4247, <https://doi.org/10.5194/acp-21-4231-2021>.
- 478 Kravitz, B., & MacMartin, D. G. (2020), Uncertainty and the basis for confidence in solar  
479 geoengineering research. *Nature Reviews Earth & Environment*, 1(1), 64-75, [https://doi.org/](https://doi.org/10.1038/s43017-019-0004-7)  
480 10.1038/s43017-019-0004-7.

- 481 Krishnamohan, K. S., & Bala, G. (2022), Sensitivity of tropical monsoon precipitation to the  
482 latitude of stratospheric aerosol injections. *Climate Dynamics*, 1-18,  
483 <https://doi.org/10.1007/s00382-021-06121-z>.
- 484 Larson, V. E., (2017). CLUBB-SILHS: A parameterization of subgrid variability in the  
485 atmosphere. arXiv:1711.03675v2 [physics.ao-ph].
- 486 MacMartin, D. G., Kravitz, B., Tilmes, S., Richter, J. H., Mills, M. J., Lamarque, J. F., ... & Vitt,  
487 F. (2017). The climate response to stratospheric aerosol geoengineering can be tailored using  
488 multiple injection locations. *Journal of Geophysical Research: Atmospheres*, 122(23), 12-574,  
489 <https://doi.org/10.1002/2017JD026868>.
- 490 MacMartin, D. G., Wang, W., Kravitz, B., Tilmes, S., Richter, J. H., & Mills, M. J. (2019),  
491 Timescale for detecting the climate response to stratospheric aerosol geoengineering. *Journal of*  
492 *Geophysical Research: Atmospheres*, 124, 1233– 1247. <https://doi.org/10.1029/2018JD028906>.
- 493 Maher, N., Milinski, S., & Ludwig, R. (2021). Large ensemble climate model simulations:  
494 introduction, overview, and future prospects for utilising multiple types of large ensemble. *Earth*  
495 *System Dynamics*, 12(2), 401-418, <https://doi.org/10.5194/esd-12-401-2021>.
- 496 Mills, M. J., Richter, J. H., Tilmes, S., Kravitz, B., MacMartin, D. G., Glanville, A. A., Tribbia J.  
497 T, Lamarque J-F., Vitt F., Schmidt A., Gettelman A., Hannay C., Bacmeister J. T., and Kinnison,  
498 D. E. (2017), Radiative and chemical response to interactive stratospheric sulfate aerosols in  
499 fully coupled CESM1(WACCM). *Journal of Geophysical Research: Atmospheres*, 122, 13,061–  
500 13,078, <https://doi.org/10.1002/2017JD027006>.

- 501 National Academies of Sciences, Engineering, and Medicine. Reflecting Sunlight:  
502 Recommendations for Solar Geoengineering Research and Research Governance. Washington,  
503 DC: *The National Academies Press.*, <https://doi.org/10.17226/25762>, 2021.
- 504 Park, S., Bretherton, C. S., & Rasch, P. J. (2014), Integrating cloud processes in the Community  
505 Atmosphere Model, version 5. *Journal of Climate*, 27(18), 6821-6856,  
506 <https://doi.org/10.1175/JCLI-D-14-00087.1>.
- 507 O'Neill, B. C., Tebaldi, C., Van Vuuren, D. P., Eyring, V., Friedlingstein, P., Hurtt, G., Knutti  
508 R., Kriegler E., Lamarque J-F., Lowe J., Meehl G. A., Moss R., Riahi K., and Sanderson B. M.,  
509 (2016) The Scenario Model Intercomparison Project (ScenarioMIP) for CMIP6. *Geoscientific  
510 Model Development*, 9(9), 3461–3482, <https://doi.org/10.5194/gmd-9-3461-2016>.
- 511 Park, S., Bretherton, C. S., & Rasch, P. J. (2014). Integrating cloud processes in the Community  
512 Atmosphere Model, version 5. *Journal of Climate*, 27(18), 6821-6856,  
513 <https://doi.org/10.1175/JCLI-D-14-00087.1>.
- 514 Paulot, F., Paynter, D., Ginoux, P., Naik, V., & Horowitz, L. W. (2018). Changes in the aerosol  
515 direct radiative forcing from 2001 to 2015: observational constraints and regional mechanisms.  
516 *Atmospheric Chemistry and Physics*, 18(17), 13265-13281, [https://doi.org/10.5194/acp-18-](https://doi.org/10.5194/acp-18-13265-2018)  
517 13265-2018.
- 518 Pinto, I., Jack, C., Lennard, C., Tilmes, S., & Odoulami, R. C. (2020), Africa's climate response  
519 to solar radiation management with stratospheric aerosol. *Geophysical Research Letters*, 47(2),  
520 e2019GL086047, <https://doi.org/10.1029/2019GL086047>.
- 521 Richter, J. H., Tilmes, S., Mills, M. J., Tribbia, J., Kravitz, B., MacMartin, D. G., Vitt, F., and  
522 Lamarque J-F. (2017), Stratospheric dynamical response and ozone feedbacks in the presence of

- 523 SO<sub>2</sub> injections. *Journal of Geophysical Research: Atmospheres*, 122, 12,557–12,573,  
524 <https://doi.org/10.1002/2017JD026912>.
- 525 Richter, J., D Visoni , D G. MacMartin , D A. Bailey , N. Rosenbloom , W. R. Lee , M. Tye , &  
526 Lamarque, J-F (2022), ARISE Assessing Responses and Impacts of Solar climate intervention on  
527 the Earth system with stratospheric aerosol injection (ARISE-SAI), *Geoscientific Model*  
528 *Development.*, submitted.
- 529 Rodgers, K. B., Lee, S. S., Rosenbloom, N., Timmermann, A., Danabasoglu, G., Deser, C., ... &  
530 Yeager, S. G. (2021), Ubiquity of human-induced changes in climate variability. *Earth System*  
531 *Dynamics*, 12(4), 1393-1411, <https://doi.org/10.5194/esd-12-1393-2021>.
- 532 Samset, B. H., Myhre, G., Forster, P. M., Hodnebrog, Ø., Andrews, T., Faluvegi, G., et al.  
533 (2016). Fast and slow precipitation responses to individual climate forcings: A PDRMIP  
534 multimodel study. *Geophysical Research Letters*, 43, 2782–2791. [https://doi.org/10.1002/](https://doi.org/10.1002/2016GL068064)  
535 [2016GL068064](https://doi.org/10.1002/2016GL068064).
- 536 Simpson, I. R., Tilmes, S., Richter, J. H., Kravitz, B., MacMartin, D. G., Mills, M. J., Fasullo J.  
537 T., and Pendergrass A. G. (2019), The regional hydroclimate response to stratospheric sulfate  
538 geoengineering and the role of stratospheric heating. *Journal of Geophysical Research:*  
539 *Atmospheres*, 124, 12587– 12616, <https://doi.org/10.1029/2019JD031093>.
- 540 Smith, W., & Wagner, G. (2018), Stratospheric aerosol injection tactics and costs in the first 15  
541 years of deployment. *Environmental Research Letters*, 13(12), 124001,  
542 <https://doi.org/10.1088/1748-9326/aae98d>.
- 543 Smith, R., Jones P., Briegleb B., Bryan F., Danabasoglu G., Dennis J., Dukowicz J., Eden C.,  
544 Fox-Kemper B., Gent P., Hecht M., Jayne S., Jochum M., Large W., Lindsay K., Maltrud M.,

- 545 Norton N., Peacock S., Vertenstein M., Year S. (2010), The Parallel Ocean Program (POP)  
546 reference manual, Ocean component of the Community Climate System Model (CCSM), LANL  
547 Technical Report, LAUR-10-01853, 141 pp.
- 548 Sun, W., Wang, B., Chen, D., Gao, C., Lu, G., & Liu, J. (2020), Global monsoon response to  
549 tropical and Arctic stratospheric aerosol injection. *Climate Dynamics*, 55(7), 2107-2121,  
550 <https://doi.org/10.1007/s00382-020-05371-7>.
- 551 Tilmes, S., Fasullo, J., Lamarque, J. F., Marsh, D. R., Mills, M., Alterskjær, K., ... & Watanabe,  
552 S. (2013). The hydrological impact of geoengineering in the Geoengineering Model  
553 Intercomparison Project (GeoMIP). *Journal of Geophysical Research: Atmospheres*, 118(19),  
554 11-036, doi: 10.1002/jgrd.50868.
- 555 Tilmes, S., Richter, J. H., Kravitz, B., MacMartin, D. G., Mills, M. J., Simpson, I. R., ... &  
556 Ghosh, S. (2018), CESM1 (WACCM) stratospheric aerosol geoengineering large ensemble  
557 project. *Bulletin of the American Meteorological Society*, 99(11), 2361-2371,  
558 <https://doi.org/10.1175/BAMS-D-17-0267.1>.
- 559 Tilmes, S., MacMartin, D. G., Lenaerts, J., Van Kampenhout, L., Muntjewerf, L., Xia, L., ... &  
560 Robock, A. (2020), Reaching 1.5 and 2.0 C global surface temperature targets using stratospheric  
561 aerosol geoengineering. *Earth System Dynamics*, 11(3), 579-601, [https://doi.org/10.5194/esd-11-](https://doi.org/10.5194/esd-11-579-2020)  
562 579-2020.
- 563 Visioni, D., MacMartin, D. G., Kravitz, B., Boucher, O., Jones, A., Lurton, T., ... & Tilmes, S.  
564 (2021), Identifying the sources of uncertainty in climate model simulations of solar radiation  
565 modification with the G6sulfur and G6solar Geoengineering Model Intercomparison Project

- 566 (GeoMIP) simulations. *Atmospheric Chemistry and Physics*, 21(13), 10039-10063,  
567 <https://doi.org/10.5194/acp-21-10039-2021>.
- 568 Visioni, D., Bednarz, E. M., Lee, W. R., Kravitz, B., Jones, A., Haywood, J. M., and MacMartin,  
569 D. G.: Climate response to off-equatorial stratospheric sulfur injections in three Earth System  
570 Models - Part 1: experimental protocols and surface changes, EGU sphere,  
571 <https://doi.org/10.5194/egusphere-2022-401>, 2022.
- 572 Wang, Z., Lin, L., Xu, Y., Che, H., Zhang, X., Zhang, H., ... & Xie, B. (2021). Incorrect Asian  
573 aerosols affecting the attribution and projection of regional climate change in CMIP6  
574 models. *NPJ Climate and Atmospheric Science*, 4(1), 1-8, [https://doi.org/10.1038/s41612-020-](https://doi.org/10.1038/s41612-020-00159-2)  
575 [00159-2](https://doi.org/10.1038/s41612-020-00159-2).
- 576 Xie, M., Moore, J. C., Zhao, L., Wolovick, M., & Muri, H. (2021), Impacts of three types of  
577 solar geoengineering on the North Atlantic Meridional Overturning Circulation. *Atmospheric*  
578 *Chemistry and Physics Discussions*, 1-28, <https://doi.org/10.5194/acp-2021-877>.
- 579 Xu, Y., Lin, L., Tilmes, S., Dagon, K., Xia, L., Diao, C., ... & Burnell, L. (2020), Climate  
580 engineering to mitigate the projected 21st-century terrestrial drying of the Americas: Carbon  
581 Capture vs. Sulfur Injection. *Earth System Dynamics*, <https://doi.org/10.5194/esd-2020-2>.
- 582 Zhang, R. R. Sutton, G. Danabasoglu, Y.-O. Kwon, R. Marsh, S. G. Yeager, D. E. Amrhein, C.  
583 M. Little, (2019), A review of the role of the Atlantic meridional overturning circulation in  
584 Atlantic multidecadal variability and associated climate impacts. *Rev. Geophys.* **57**, 316–375  
585 (2019), <https://doi.org/10.1029/2019RG000644>.
- 586 Zhang, Q., Chang, P., Yeager, S. G., Danabasoglu, G., & Zhang, S. (2022), Role of sea-surface  
587 salinity in simulating historical decadal variations of Atlantic meridional overturning circulation

588 in a coupled climate model. *Geophysical Research Letters*, 49, e2021GL096922.

589 <https://doi.org/10.1029/2021GL096922>.

590 Zhao, M., Cao, L., Bala, G., & Duan, L. (2021), Climate response to latitudinal and altitudinal

591 distribution of stratospheric sulfate aerosols. *Journal of Geophysical Research: Atmospheres*,

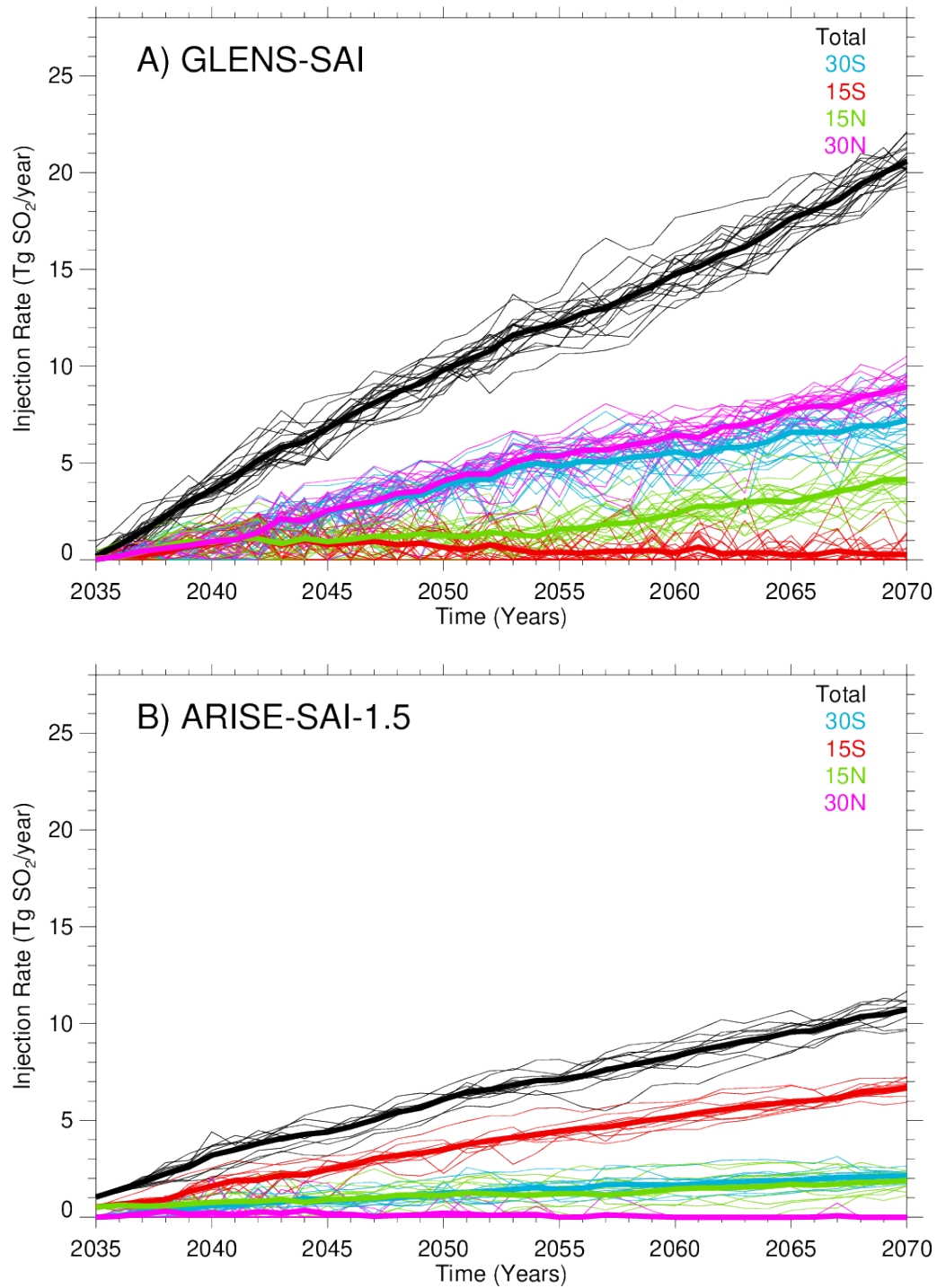
592 126, e2021JD035379. <https://doi.org/10.1029/2021JD035379>

593

594 Table 1. Climate model experiments used in this study and their design characteristics.

Ensemble Name	Lateral Resolution	Vertical Levels	# mem	Time Span	Future Scenario	Notes
CESM1-WACCM5-RCP85	0.9°x1.25°	70	20 (3*)	2006-2030 (2099)	RCP85	*3 members extend to 2099
GLENS-SAI	0.9°x1.25°	70	20	2020-2097	RCP85+SAI	
CESM2-WACCM6-SSP585	0.9°x1.25°	70	5		SSP585	
ARISE-SAI-1.5	0.9°x1.25°	70	10	2035-2069	SSP245+SAI	
CESM1-LE	0.9°x1.25°	30	40	1920-2100	RCP85	
CESM2-LE	0.9°x1.25°	32	50	1850-2100	SSP370	*smoothed biomass emissions
CESM2-RCP85	0.9°x1.25°	32	10	1920-2100	RCP85	
CESM1-AMIP	0.9°x1.25°	30	1	1979-2005	N/A	
CESM1-4xCO2AMIP	0.9°x1.25°	30	1	1979-2005	N/A	
CESM2-AMIP	0.9°x1.25°	32	1	1979-2014	N/A	
CESM2-4xCO2AMIP	0.9°x1.25°	32	1	1979-2014	N/A	
CESM2-AMIP+4K	0.9°x1.25°	32	1	1979-2014	N/A	
CESM1-PI	0.9°x1.25°	30	1	0-1800	N/A	
CESM2-PI	0.9°x1.25°	30	1	0-2000	N/A	
CESM1-Abrupt4xCO2	0.9°x1.25°	32	1	0-150	N/A	
CESM2-Abrupt4xCO2	0.9°x1.25°	32	1	0-150	N/A	

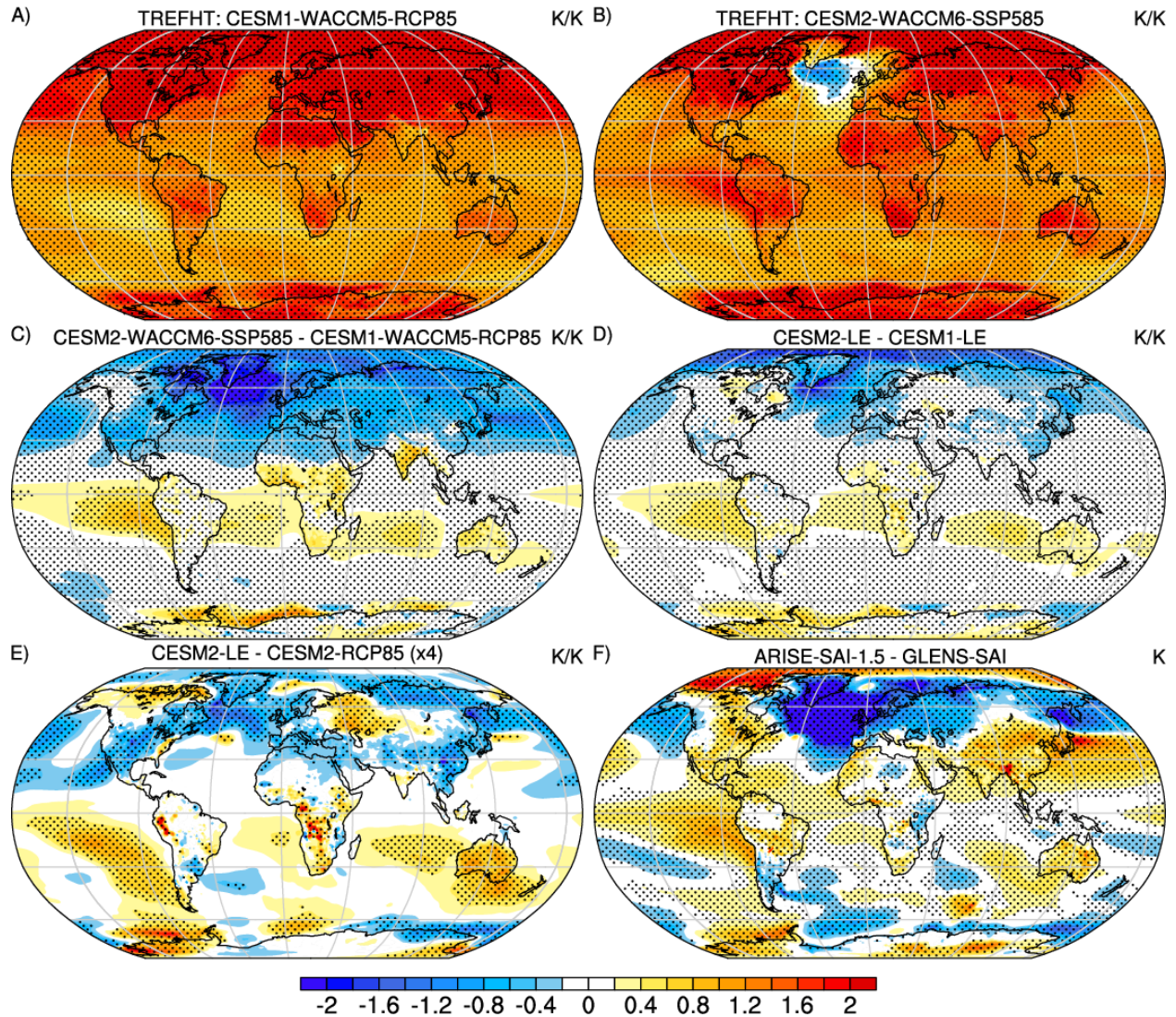
596



597

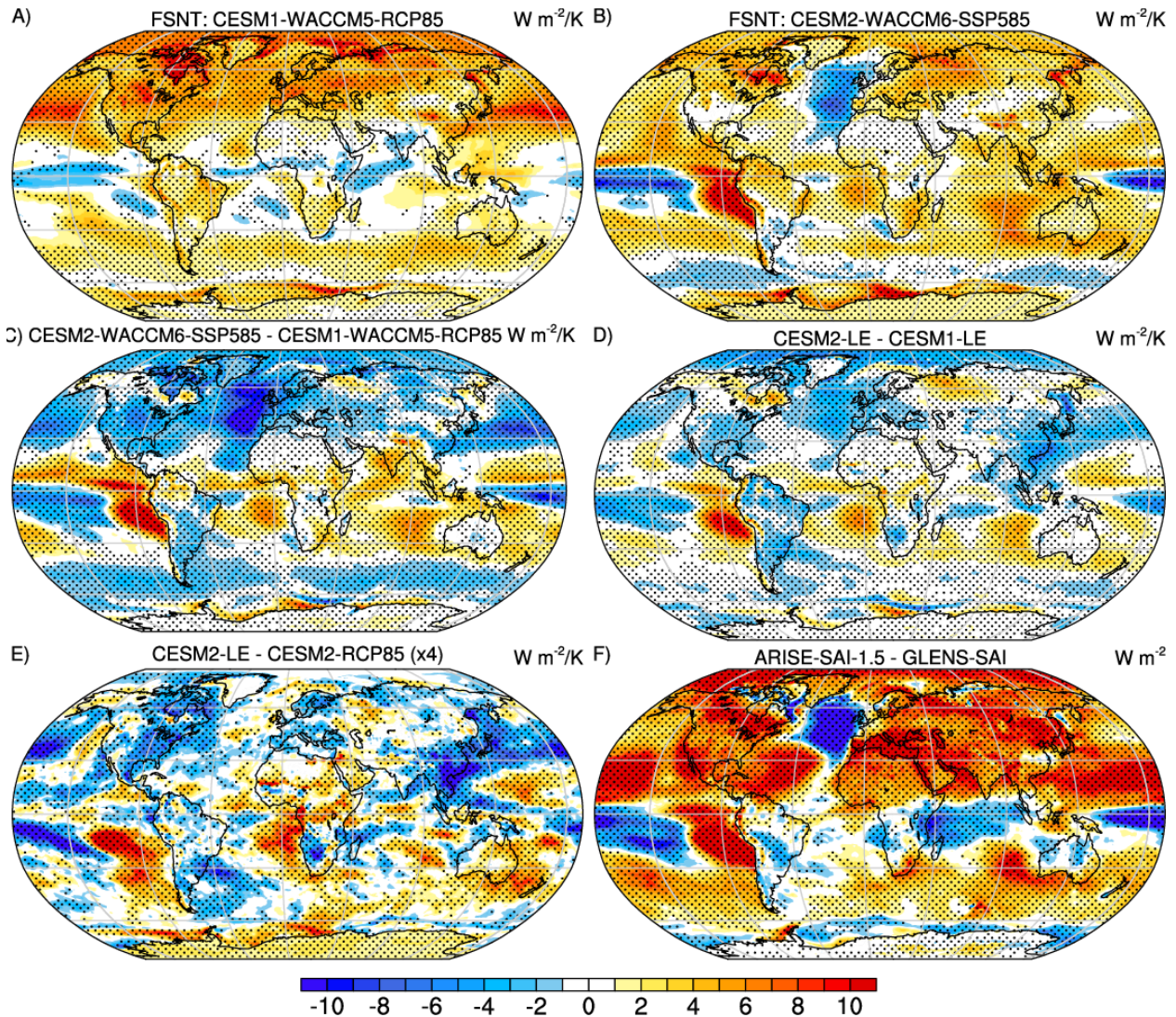
598 **Figure 1.** Evolution of yearly sulfur dioxide injections (Tg SO<sub>2</sub> yr<sup>-1</sup>) over time at the four

599 injection latitudes for (a) GLENS-SAI and (b) ARISE-SAI-1.5 from 2035 to 2070.



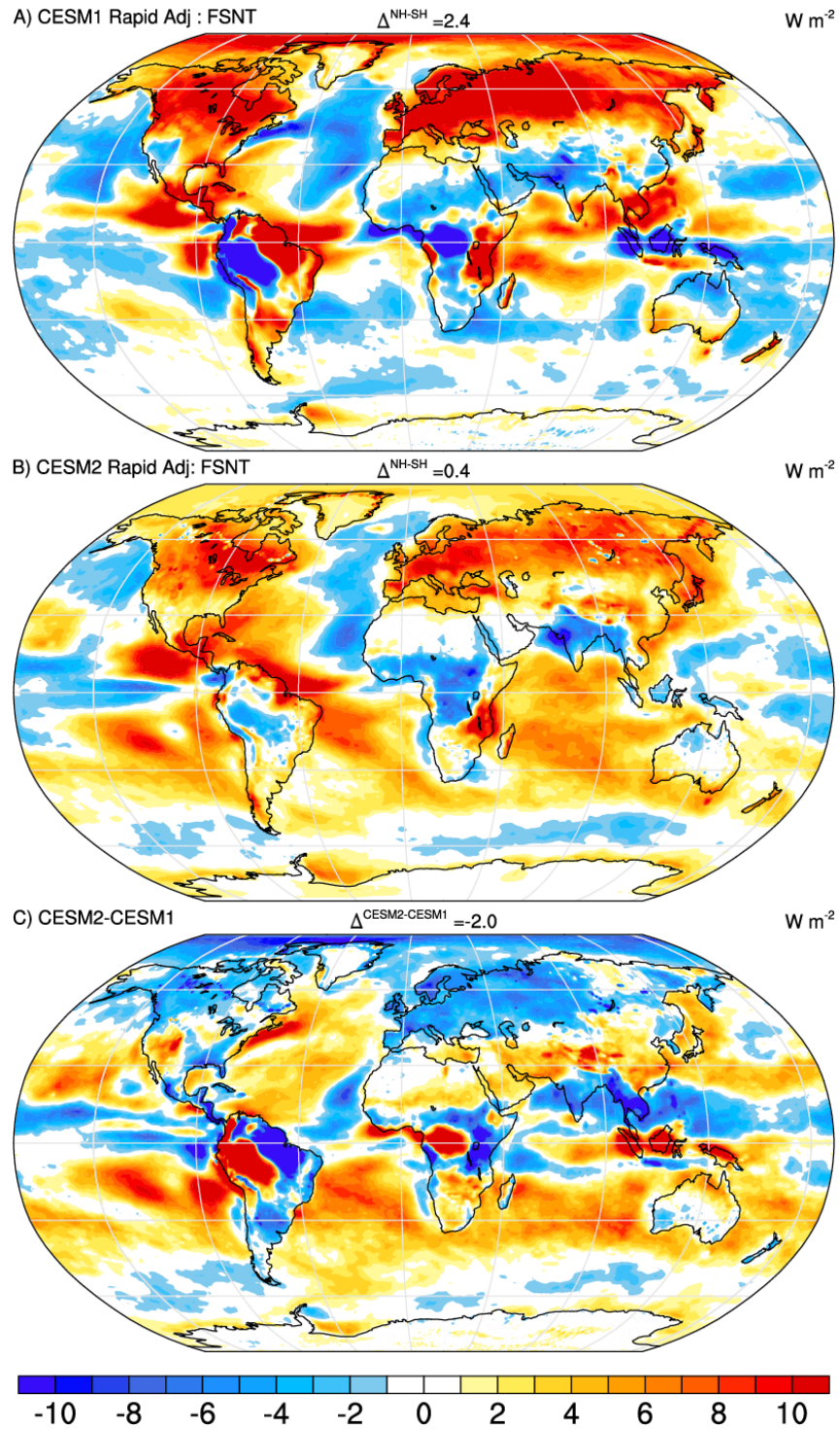
600

601 **Figure 2.** Normalized response in near surface air temperature (TREFHT) estimated from the  
 602 change between 2020-39 and 2050-69 per degree global warming for unmitigated (a) CESM1-  
 603 WACCM5-RCP85 and (b) CESM2-WACCM6-SSP585 simulations, and (c) their difference (b-  
 604 a). Also shown is (d) the analogous difference for the CESM1-LE and CESM2-LE and (e) the  
 605 CESM2-RCP85 and CESM2-LE (scaled by 4). The difference between the geoengineered  
 606 climate states in ARISE-SAI-1.5 and GLENS-SAI is shown in (f). Units for all panels are  $\text{K K}^{-1}$ ,  
 607 except in (f) where units are  $\text{W m}^{-2}$ , and stippled regions indicate differences that exceed twice  
 608 the ensemble standard error.



609

610 **Figure 3.** Normalized response in net top-of-atmosphere radiation (FSNT) estimated from the  
 611 change between 2020-39 and 2050-69 per degree global warming for unmitigated (a) CESM1-  
 612 WACCM5-RCP85 and (b) CESM2-WACCM6-SSP585 simulations, and (c) their difference (b-  
 613 a). Also shown is (d) the analogous difference for the CESM1-LE and CESM2-LE and (e) the  
 614 CESM2-RCP85 and CESM2-LE (scaled by 4). The difference between the geoengineered  
 615 climate states in ARISE-SAI-1.5 and GLENS-SAI is shown in (f). Units for all panels are  $W m^{-2}$   
 616  $K^{-1}$ , except in (f) where units are  $W m^{-2}$ , and stippled regions indicate differences that exceed  
 617 twice the ensemble standard error.

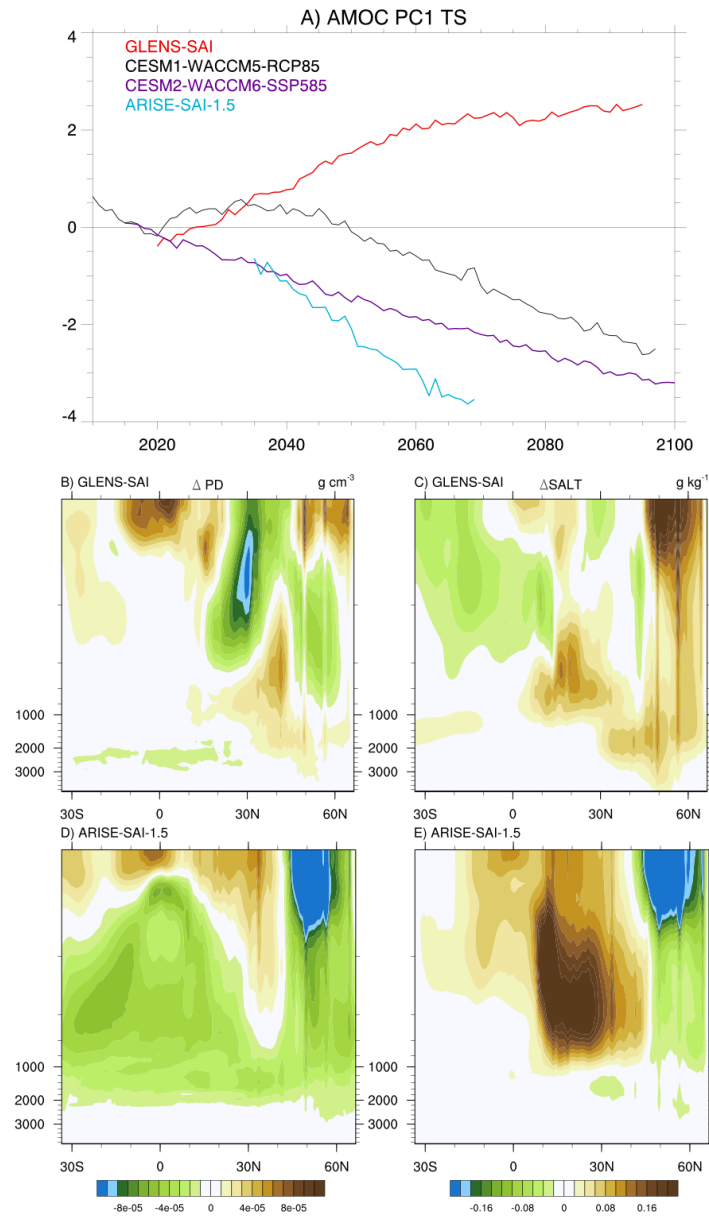


618

619 Figure 4: Estimates of the rapid adjustment of TOA net SW flux to CO<sub>2</sub> for CESM1 (a), CESM2

620 (b), and their difference (c) based on estimates from 4xCO<sub>2</sub>AMIP and AMIP simulations.

621 Differences in the hemispheric means are shown in panel titles. All units are W m<sup>-2</sup>.



622

623 **Figure 5.** (a) Changes in the leading principal component of the Atlantic Meridional Overturning

624 Circulation in unmitigated (CESM1-WACCM5-RCP85, CESM2-WACCM6-SSP585) and

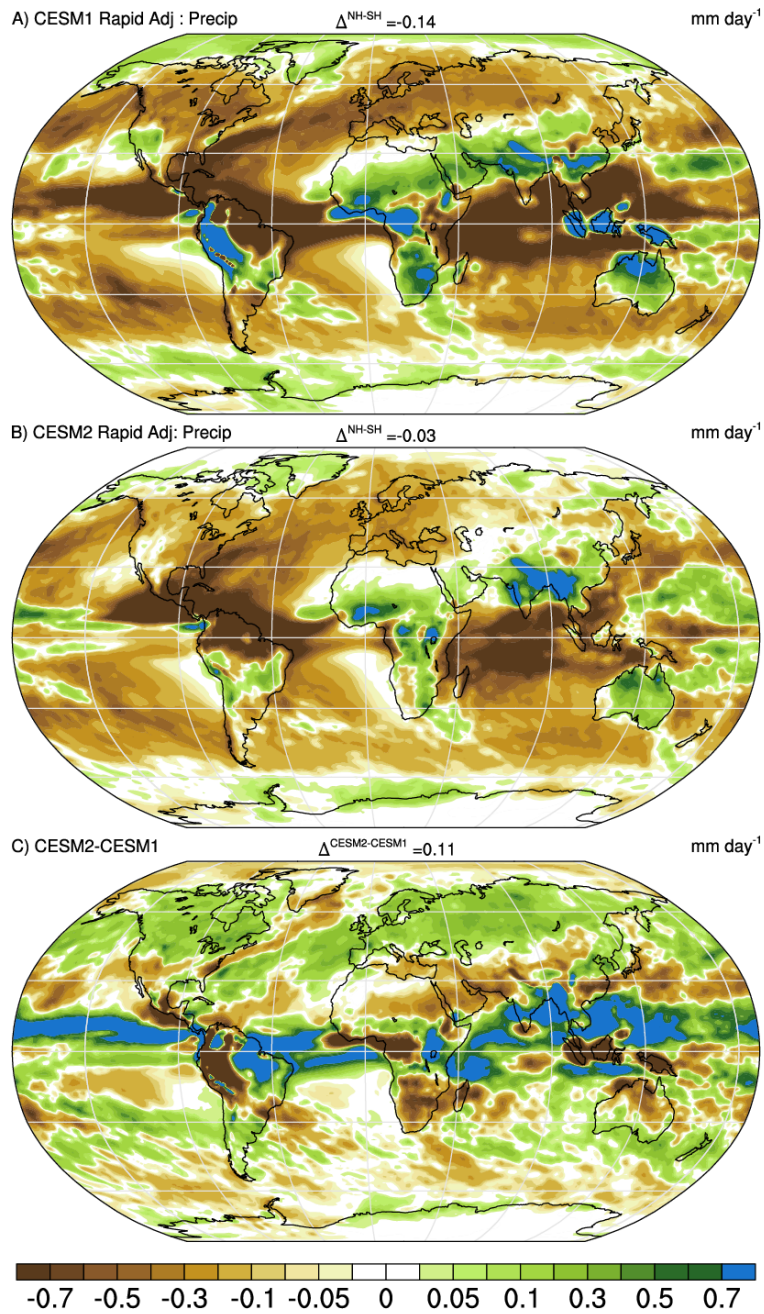
625 mitigated (GLENS-SAI, ARISE-SAI-1.5) experiments. Also shown are changes in the latitude-

626 depth structure in the Atlantic Ocean of ocean potential density (PD, b, d, units of  $g\ cm^{-3}$ ) and

627 salinity (SALT, c, e, units of  $g\ kg^{-1}$ ) for GLENS-SAI (b, c) and ARISE-SAI-1.5 (d, e),

628 respectively.

629

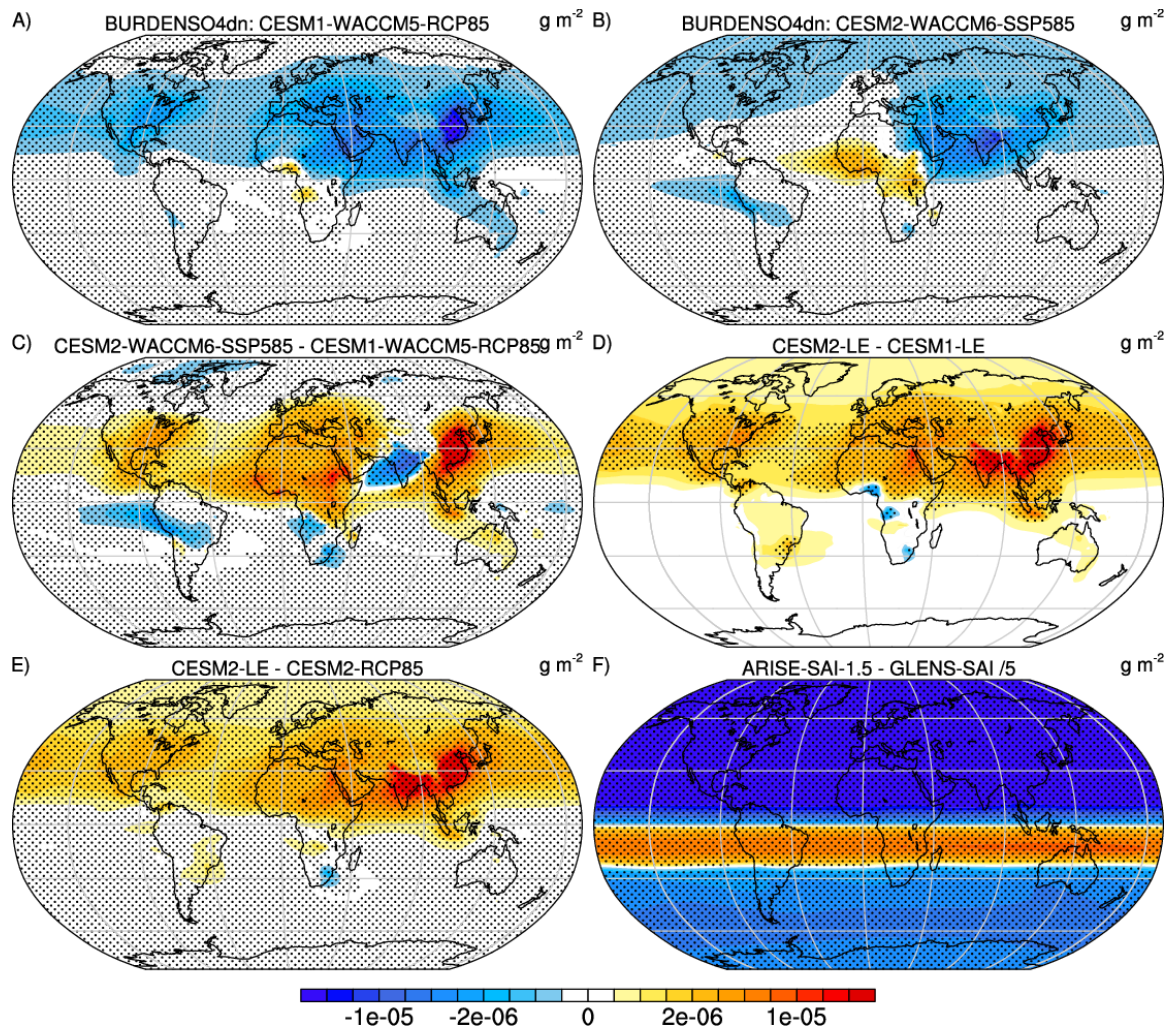


630

631 Figure 6: The rapid adjustment of total precipitation to CO<sub>2</sub> quadrupling for CESM1 (a), CESM2

632 (b), and their difference (c) based on estimates from 4xCO<sub>2</sub>AMIP and AMIP simulations.

633 Differences in the hemispheric means are shown in panel titles. All units are mm day<sup>-1</sup>.



634

635 **Figure 7.** Absolute change in sulfate aerosol burdens (BURDENSO4dn) estimated from the difference  
 636 between 2020-39 and 2050-69 for unmitigated (a) CESM1-WACCM5-RCP85 and (b) CESM2-  
 637 WACCM6-SSP585 simulations, and (c) their difference (b-a). Also shown is (d) the analogous difference  
 638 for the CESM1-LE and CESM2-LE and (e) the CESM2-RCP85 and CESM2-LE. The difference between  
 639 the geoengineered climate states in ARISE-SAI-1.5 and GLENS-SAI is shown in (f). Units for all panels  
 640 are  $\text{g m}^{-2}$  and stippled regions indicate differences that exceed twice the ensemble standard error. The  
 641 difference field in (f) is scaled by  $1/5^{\text{th}}$ .

642

643

644 **Figure Captions**

645 **Figure 1.** Evolution of yearly injection mass ( $\text{Tg SO}_2 \text{ yr}^{-1}$ ) over time at the four injection  
 646 latitudes for (a) GLENS-SAI and (b) ARISE-SAI-1.5 from 2035 to 2070.

647 **Figure 2.** Normalized response in near surface air temperature (TREFHT) estimated from the  
 648 change between 2020-39 and 2050-69 per degree global warming for unmitigated (a) CESM1-  
 649 WACCM5-RCP85 and (b) CESM2-WACCM6-SSP585 simulations, and (c) their difference (b-  
 650 a). Also shown is (d) the analogous difference for the CESM1-LE and CESM2-LE and (e) the  
 651 CESM2-RCP85 and CESM2-LE (scaled by 4). The difference between the geoengineered  
 652 climate states in ARISE-SAI-1.5 and GLENS-SAI is shown in (f). Units for all panels are  $\text{K K}^{-1}$ ,  
 653 except in (f) where units are  $\text{W m}^{-2}$ , and stippled regions indicate differences that exceed twice  
 654 the ensemble standard error.

655 **Figure 3.** Normalized response in net top-of-atmosphere radiation (FSNT) estimated from the  
 656 change between 2020-39 and 2050-69 per degree global warming for unmitigated (a) CESM1-  
 657 WACCM5-RCP85 and (b) CESM2-WACCM6-SSP585 simulations, and (c) their difference (b-  
 658 a). Also shown is (d) the analogous difference for the CESM1-LE and CESM2-LE and (e) the  
 659 CESM2-RCP85 and CESM2-LE (scaled by 4). The difference between the geoengineered  
 660 climate states in ARISE-SAI-1.5 and GLENS-SAI is shown in (f). Units for all panels are  $\text{W m}^{-2}$   
 661  $\text{K}^{-1}$ , except in (f) where units are  $\text{W m}^{-2}$ , and stippled regions indicate differences that exceed  
 662 twice the ensemble standard error.

663 **Figure 4.** Estimates of the rapid adjustment of TOA net SW flux to  $\text{CO}_2$  for CESM1 (a), CESM2  
 664 (b), and their difference (c) based on estimates from 4x $\text{CO}_2$ AMIP and AMIP simulations.  
 665 Differences in the hemispheric means are shown in panel titles. All units are  $\text{W m}^{-2}$ .

666 **Figure 5.** (a) Changes in the leading principal component of the Atlantic Meridional Overturning  
 667 Circulation in unmitigated (CESM1-WACCM5-RCP85, CESM2-WACCM6-SSP585) and  
 668 mitigated (GLENS-SAI, ARISE-SAI-1.5) experiments. Also shown are changes in the latitude-  
 669 depth structure in the Atlantic Ocean of ocean potential density (PD, b, d, units of  $\text{g cm}^{-3}$ ) and  
 670 salinity (SALT, c, e, units of  $\text{g kg}^{-1}$ ) for GLENS-SAI (b, c) and ARISE-SAI-1.5 (d, e),  
 671 respectively.

672 **Figure 6.** The rapid adjustment of total precipitation to  $\text{CO}_2$  quadrupling for CESM1 (a),  
 673 CESM2 (b), and their difference (c) based on estimates from 4x $\text{CO}_2$ AMIP and AMIP  
 674 simulations. Differences in the hemispheric means are shown in panel titles. All units are  $\text{mm}$   
 675  $\text{day}^{-1}$ .

676 **Figure 7.** Absolute change in sulfate aerosol burdens (BURDEN $\text{SO}_4$ dn) estimated from the difference  
 677 between 2020-39 and 2050-69 for unmitigated (a) CESM1-WACCM5-RCP85 and (b) CESM2-  
 678 WACCM6-SSP585 simulations, and (c) their difference (b-a). Also shown is (d) the analogous difference  
 679 for the CESM1-LE and CESM2-LE and (e) the CESM2-RCP85 and CESM2-LE. The difference between  
 680 the geoengineered climate states in ARISE-SAI-1.5 and GLENS-SAI is shown in (f). Units for all panels  
 681 are  $\text{g m}^{-2}$  and stippled regions indicate differences that exceed twice the ensemble standard error. The  
 682 difference field in (f) is scaled by  $1/5^{\text{th}}$ .

683 **Figure S1:** Normalized response in net top-of-atmosphere radiative flux (RTMT) estimated from the  
 684 change between 2020-39 and 2050-69 per degree global warming for unmitigated (a) CESM1-

685 WACCM5-RCP85 and (b) CESM2-WACCM6-SSP585 simulations, and (c) their difference (b-a). Also  
686 shown is (d) the analogous difference for the CESM1-LE and CESM2-LE and (e) the CESM2-RCP85  
687 and CESM2-LE (scaled by 4). The difference between the geoengineered climate states in ARISE-SAI-  
688 1.5 and GLENS-SAI is shown in (f). Units for all panels are  $\text{W m}^{-2} \text{K}^{-1}$ , except in (f) where units are  $\text{W m}^{-2}$ ,  
689 and stippled regions indicate differences that exceed twice the ensemble standard error.

690 **Figure S2:** Normalized response in outgoing top-of-atmosphere longwave flux (FLNT) per degree  
691 global warming estimated from the change between 2020-39 and 2050-69 for unmitigated (a) CESM1-  
692 WACCM5-RCP85 and (b) CESM2-WACCM6-SSP585 simulations, and (c) their difference (b-a). Also  
693 shown is (d) the analogous difference for the CESM1-LE and CESM2-LE and (e) the CESM2-RCP85  
694 and CESM2-LE (scaled by 4). The difference between the geoengineered climate states in ARISE-SAI-  
695 1.5 and GLENS-SAI is shown in (f). Units for all panels are  $\text{W m}^{-2} \text{K}^{-1}$ , except in (f) where units are  $\text{W m}^{-2}$ ,  
696 and stippled regions indicate differences that exceed twice the ensemble standard error.

697 **Figure S3:** Rapid adjustments of cloud amount (%) to  $\text{CO}_2$  based on 4x $\text{CO}_2$ AMIP-AMIP simulation  
698 differences in (a) CESM1, (b) CESM2, and (c) their difference (b-a).

699 **Figure S4:** Slow responses of FSNT ( $\text{W m}^{-2}$ ) to  $\text{CO}_2$  estimated from abrupt4x $\text{CO}_2$  simulations in  
700 CESM1 (a), and computed directly from AMIP+4K-AMIP simulation differences in CESM2 (b). The  
701 hemispheric contrasts are large for CESM1 ( $-2.3 \text{ W m}^{-2}$ ) and small for CESM2 ( $0.1 \text{ W m}^{-2}$ ).

702 **Figure S5:** Timeseries of hemispheric mean fluxes (a) and their differences (b) in abrupt4x $\text{CO}_2$   
703 simulations.

704 **Figure S6:** Response in surface salinity estimated from the change between 2020-39 and 2050-  
705 69 for unmitigated (a) CESM1-WACCM5-RCP85 and (b) CESM2-WACCM6-SSP585  
706 simulations, and their difference (c). Also shown is the analogous difference for (d) the CESM1-  
707 LE and CESM2-LE (d) and (e) the CESM2-RCP85 and CESM2-LE. The difference between the  
708 geoengineered climate states in ARISE-SAI-1.5 and GLENS-SAI is shown in (f).

709 **Figure S7:** Rapid adjustments of precipitation ( $\text{mm day}^{-1}$ ) to  $\text{CO}_2$  based on 4x $\text{CO}_2$ AMIP-AMIP  
710 simulation differences in (a) CESM1, (b) CESM2, and (c) their difference (b-a).

711



*Geophysical Research Letters*

Supporting Information for

**Scenario and Model Dependence of Strategic Solar Climate Intervention in  
CESM**

**J. T. Fasullo and J. H. Richter**

National Center for Atmospheric Research, Boulder, CO, USA.

**Contents of this file**

Figures S1 to S7

**Introduction**

These supporting figures provide further insight into the radiative responses in unmitigated warming scenarios in CESM1-WACCM5-RCP85 and CESM2-WACCM6-SSP585, the CESM1-LE and CESM2-LE, CESM2-RCP85, and the target geoengineered climate state in GLENS-SAI and ARISE-SAI-1.5. They also document rapid adjustments to CO<sub>2</sub> of clouds and radiation in CESM1 and CESM2 based on idealized 4xCO<sub>2</sub>AMIP and abrupt4xCO<sub>2</sub> coupled simulations differences with AMIP and pre-industrial control simulations (see Table 1 of the main text). These figures thus provide key context for the interpretation of SAI uncertainties provided in the main text discussion.

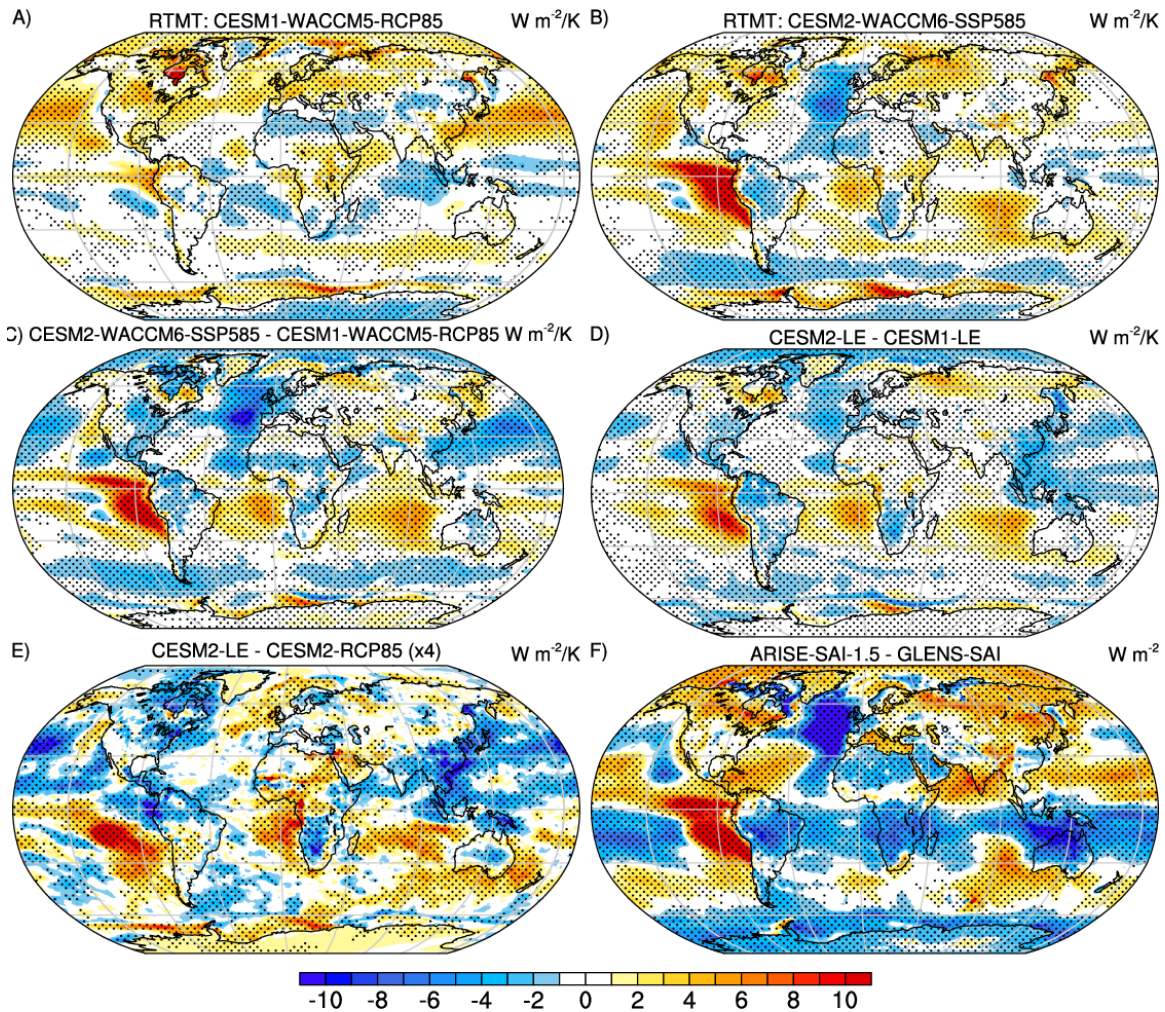


**Figure S1.** Normalized response in net top-of-atmosphere radiative flux (RTMT) estimated from the change between 2020-39 and 2050-69 per degree global warming for unmitigated (a) CESM1-WACCM5-RCP85 and (b) CESM2-WACCM6-SSP585 simulations, and (c) their difference (b-a). Also shown is (d) the analogous difference for the CESM1-LE and CESM2-LE and (e) the CESM2-RCP85 and CESM2-LE (scaled by 4). The difference between the geoengineered climate states in ARISE-SAI-1.5 and GLENS-SAI is shown in (f). Units for all panels are  $W m^{-2} K^{-1}$ , except in (f) where units are  $W m^{-2}$ , and stippled regions indicate differences that exceed twice the ensemble standard error.

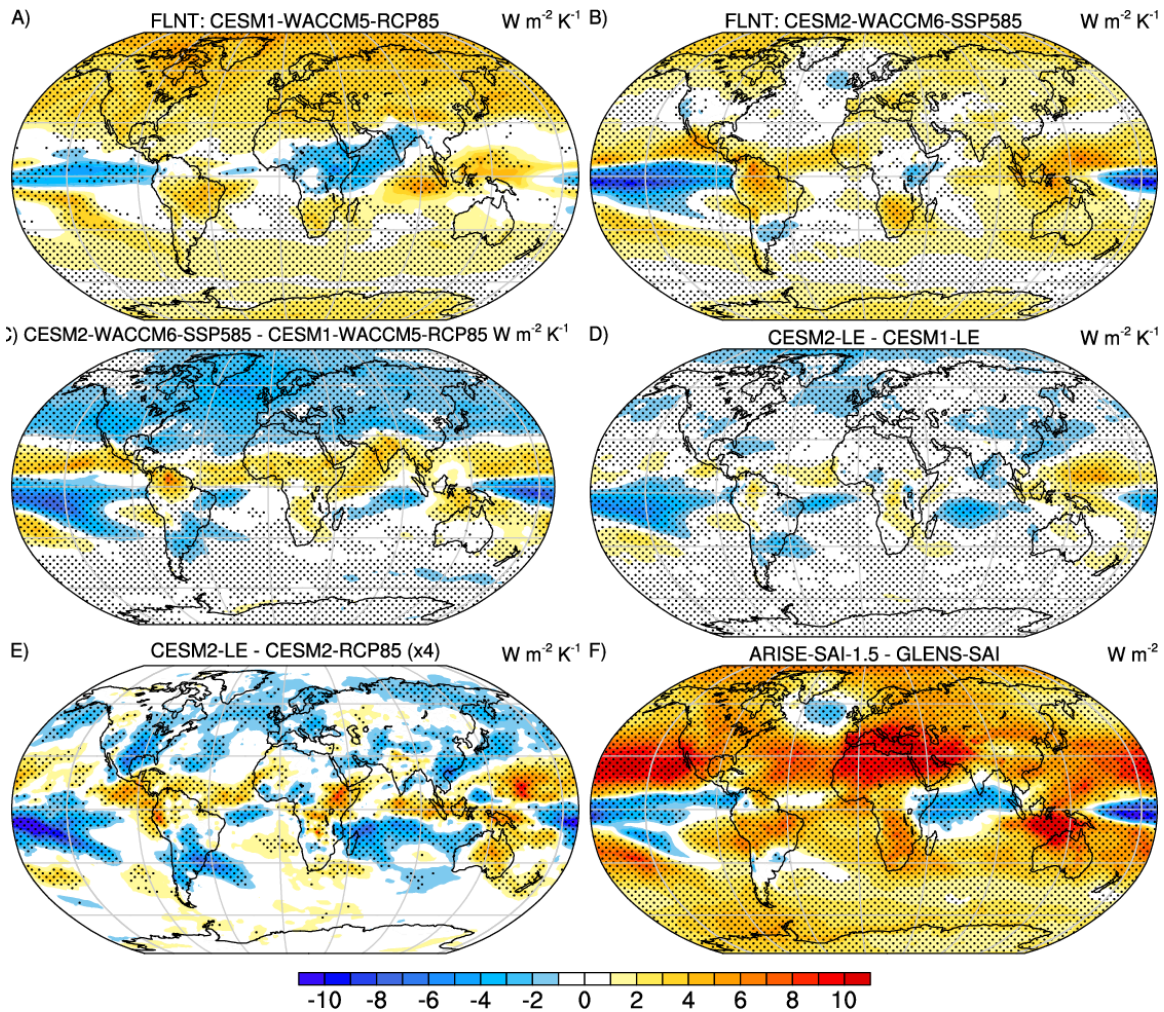


**Figure S2.** Normalized response in outgoing top-of-atmosphere longwave flux (FLNT) per degree global warming estimated from the change between 2020-39 and 2050-69 for unmitigated (a) CESM1-WACCM5-RCP85 and (b) CESM2-WACCM6-SSP585 simulations, and (c) their difference (b-a). Also shown is (d) the analogous difference for the CESM1-LE and CESM2-LE and (e) the CESM2-RCP85 and CESM2-LE (scaled by 4). The difference between the geoengineered climate states in ARISE-SAI-1.5 and GLENS-SAI is shown in (f). Units for all panels are  $\text{W m}^{-2} \text{K}^{-1}$ , except in (f) where units are  $\text{W m}^{-2}$ , and stippled regions indicate differences that exceed twice the ensemble standard error.

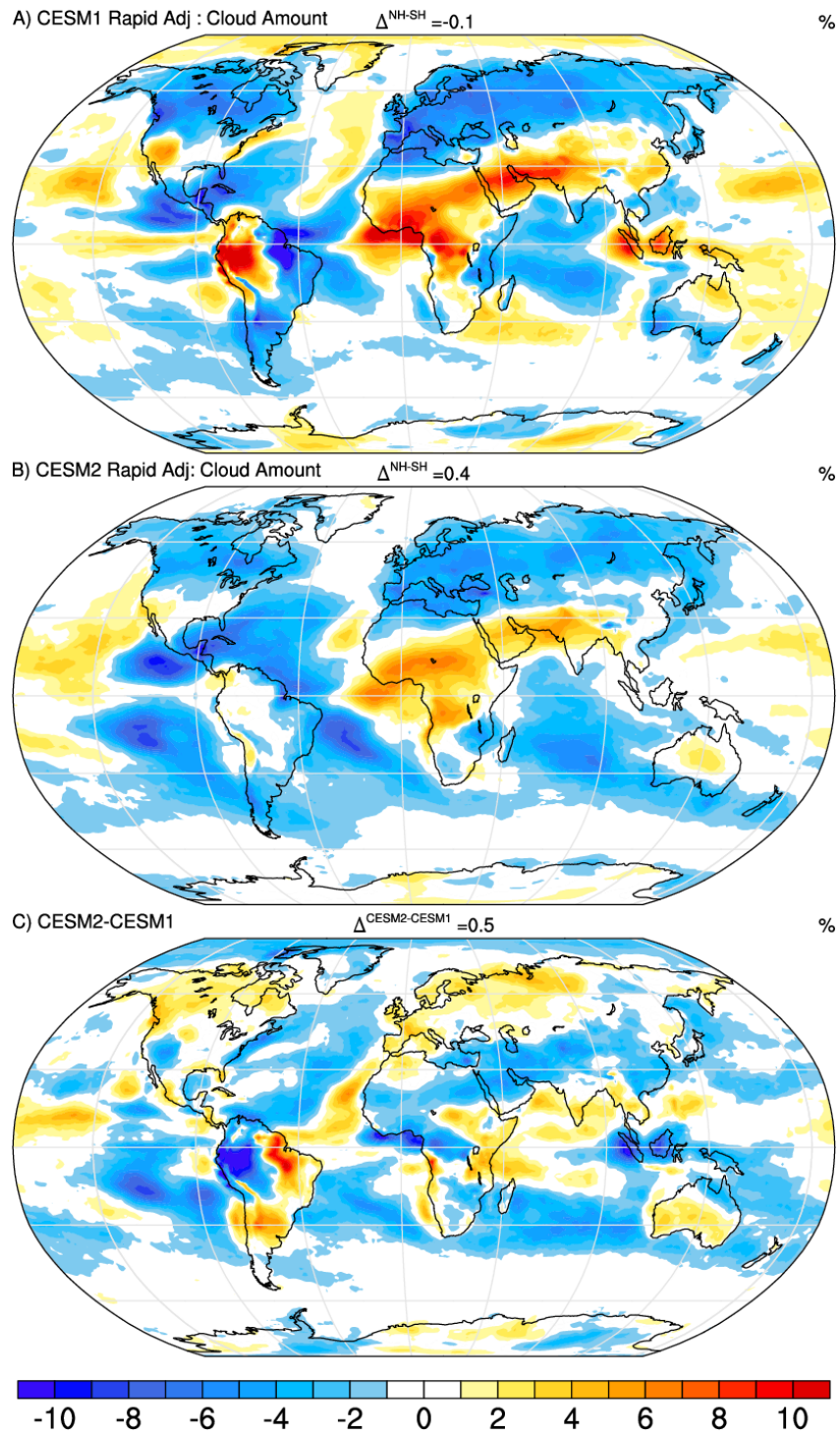
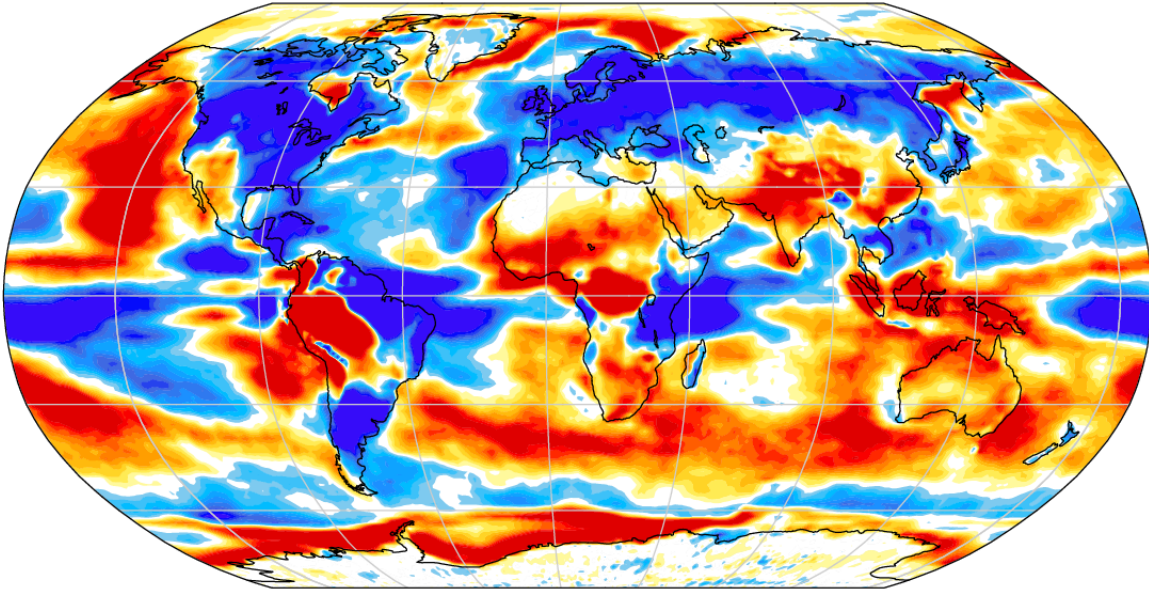


**Figure S3.** Rapid adjustments of cloud amount (%) to CO<sub>2</sub> based on 4xCO<sub>2</sub>AMIP-AMIP simulation differences in (a) CESM1, (b) CESM2, and (c) their difference (b-a).

A) CESM1 Slow Response (Est): FSNT  $\Delta^{NH-SH} = -2.3$   $W m^{-2}$



B) CESM2 Slow Response: FSNT  $\Delta^{NH-SH} = -0.1$

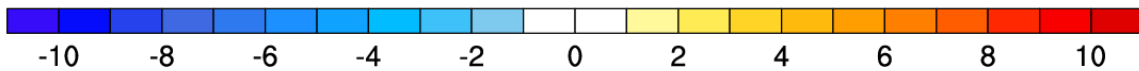
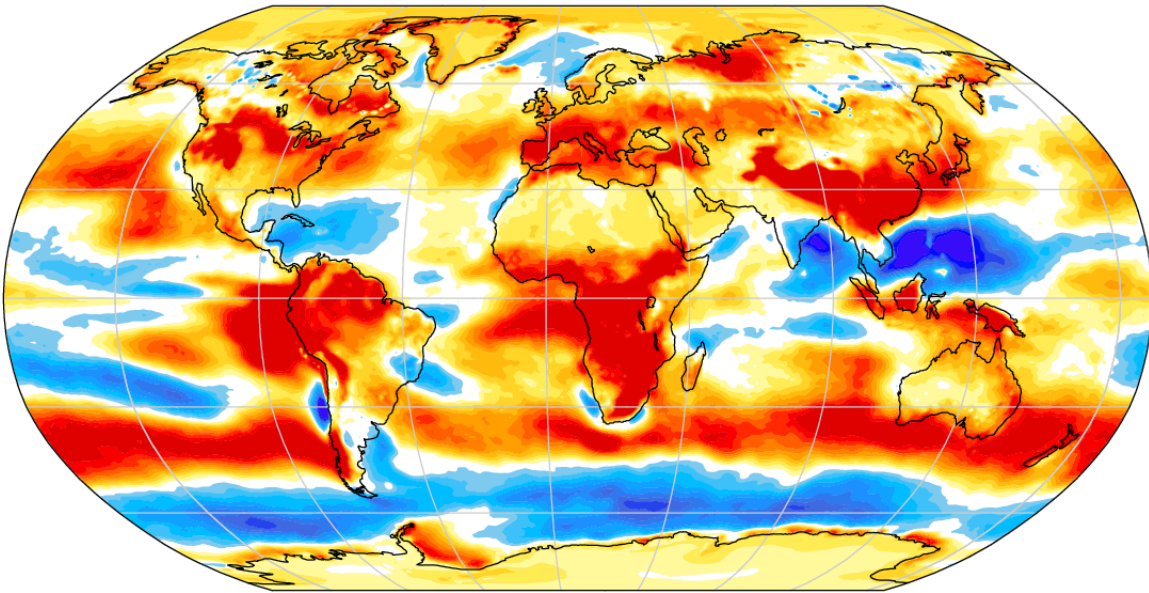


**Figure S4.** Slow responses of FSNT ( $W m^{-2}$ ) to  $CO_2$  estimated from abrupt4x $CO_2$  simulations in CESM1 (a), and computed directly from AMIP+4K-AMIP simulation differences in CESM2 (b). The hemispheric contrasts are large for CESM1 ( $-2.3 W m^{-2}$ ) and small for CESM2 ( $0.1 W m^{-2}$ ).

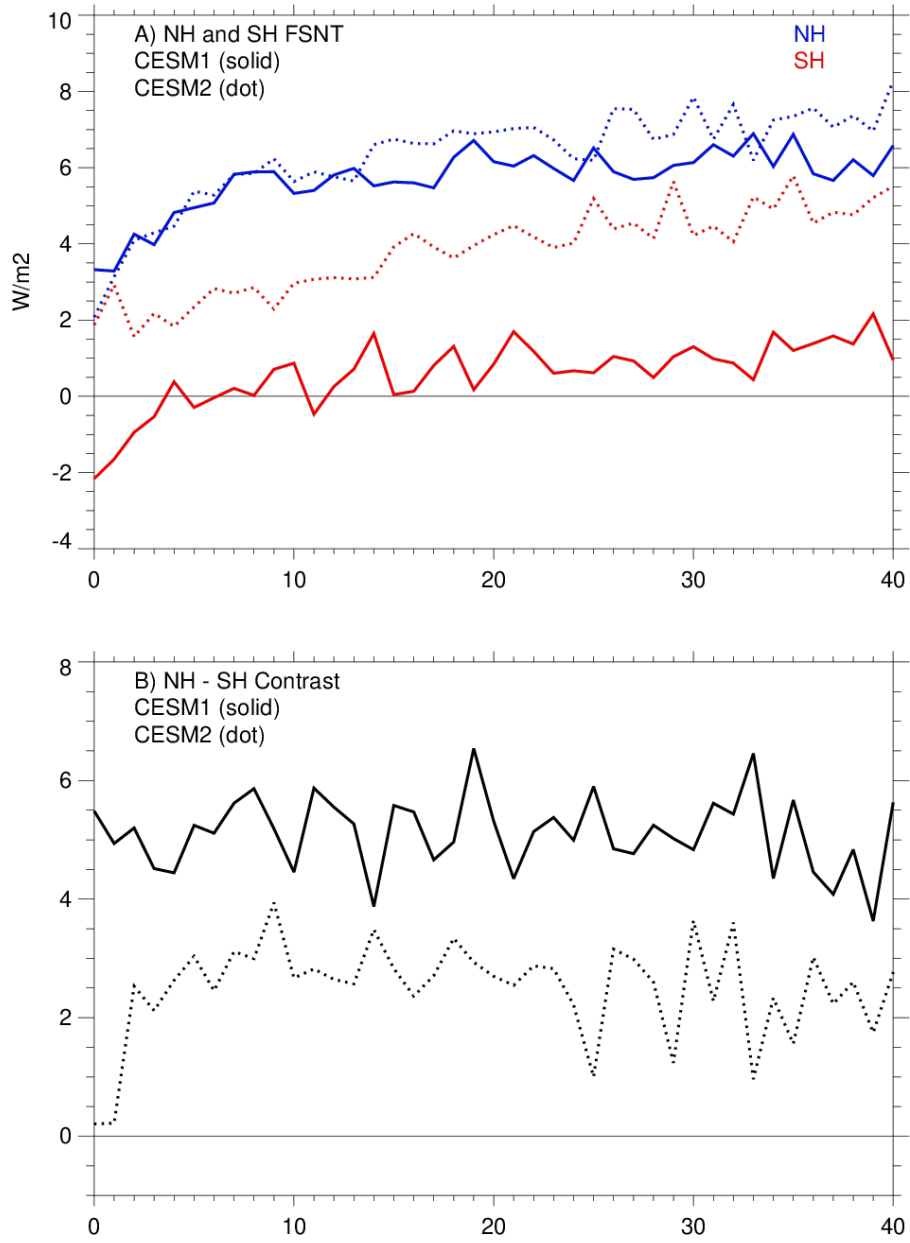


**Figure S5.** Timeseries of hemispheric mean fluxes (a) and their differences (b) in abrupt4xCO<sub>2</sub> simulations.

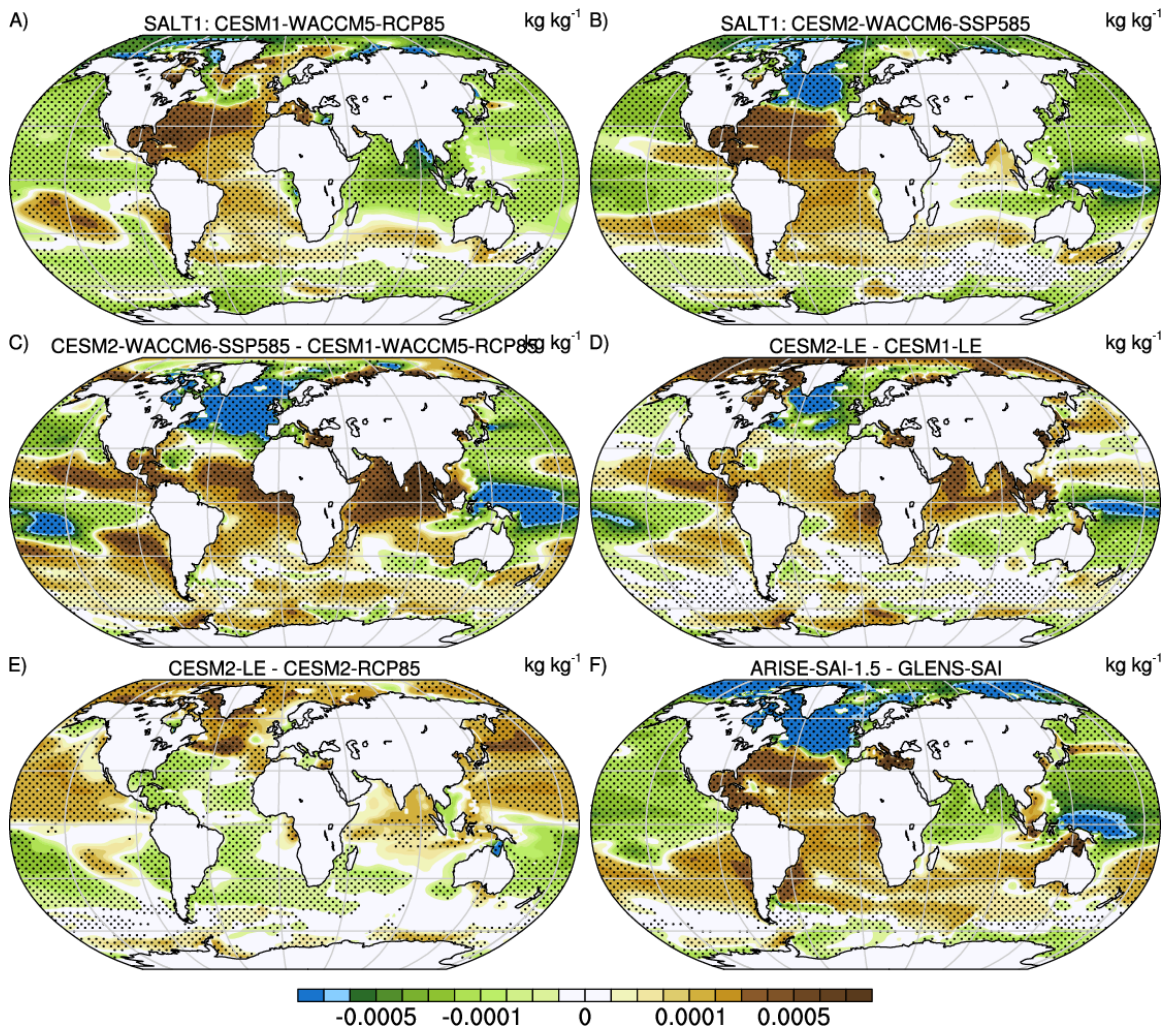
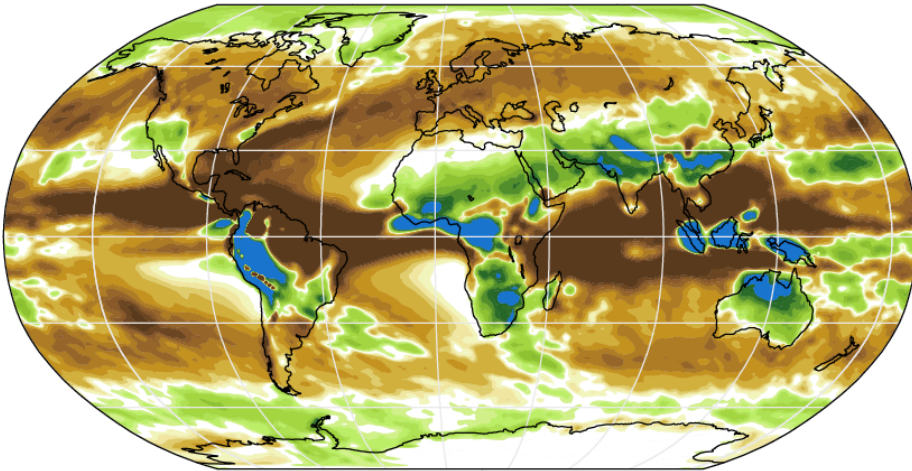
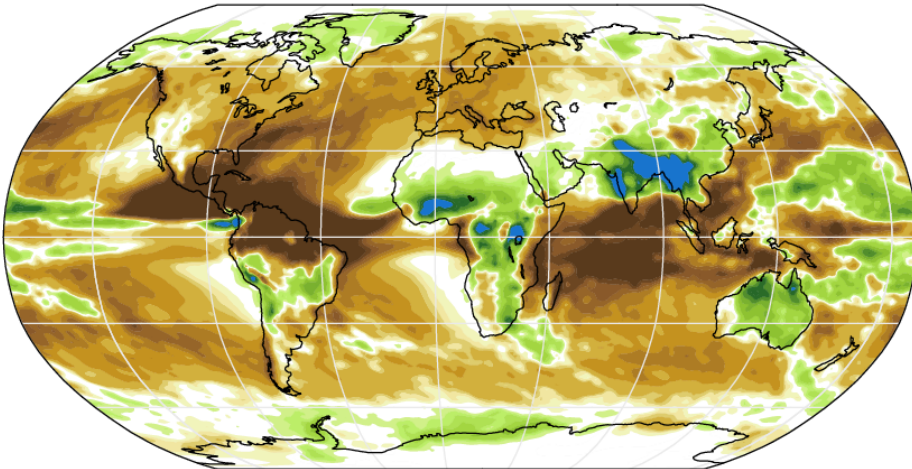


**Figure S6.** Response in surface salinity estimated from the change between 2020-39 and 2050-69 for unmitigated (a) CESM1-WACCM5-RCP85 and (b) CESM2-WACCM6-SSP585 simulations, and their difference (c). Also shown is the analogous difference for (d) the CESM1-LE and CESM2-LE (d) and (e) the CESM2-RCP85 and CESM2-LE. The difference between the geoengineered climate states in ARISE-SAI-1.5 and GLENS-SAI is shown in (f).

A) CESM1 Fast Res: Precip -0.3 (NH), -0.2 (SH) mm day<sup>-1</sup>



B) CESM2 Fast Res: Precip -0.2 (NH), -0.2 (SH) mm day<sup>-1</sup>



C) CESM2-CESM1 0.1 (NH), 0.0 (SH) mm day<sup>-1</sup>

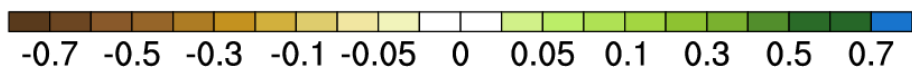
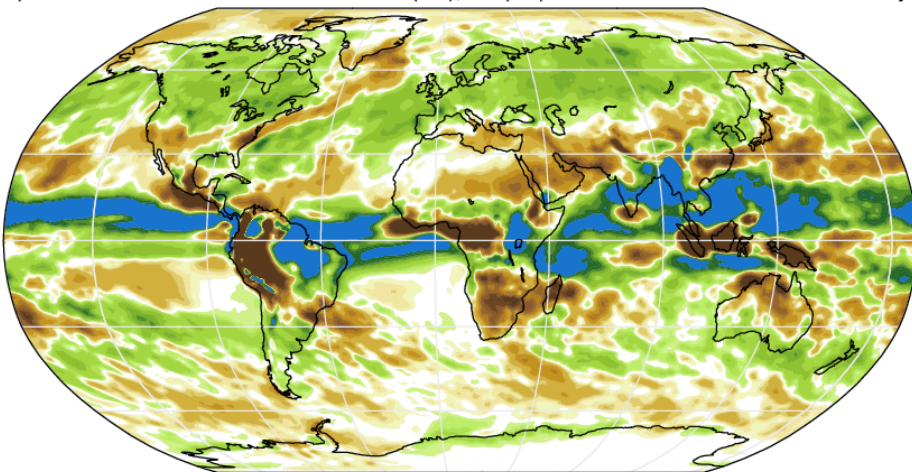


**Figure S7.** Rapid adjustments of precipitation (mm day<sup>-1</sup>) to CO<sub>2</sub> based on 4xAMIP-AMIP simulation differences in (a) CESM1, (b) CESM2, and (c) their difference (b-a).